

3 Fermi Large Area Telescope Fourth Source Catalog

4 THE *Fermi*-LAT COLLABORATION

5 ABSTRACT

6 We distribute a preliminary version of the fourth *Fermi* Large Area Telescope
 7 source catalog (4FGL) meant to help in writing 2019 NASA *Fermi* Guest Investigator
 8 proposals. This supersedes the FL8Y source list distributed in 2018^a).

9 Based on the first eight years of science data from the *Fermi* Gamma-ray Space
 10 Telescope mission and the 50 MeV–1 TeV range, it is the deepest yet in this energy range.
 11 Relative to the 3FGL catalog, the 4FGL catalog has twice as much exposure as well
 12 as a number of analysis improvements, including an updated model for Galactic diffuse
 13 γ -ray emission. The 4FGL catalog includes 5098 sources above 4σ significance, for
 14 which we provide localization and spectral properties. Seventy-five sources are modeled
 15 explicitly as spatially extended, and overall 357 sources are considered as identified
 16 based on angular extent or correlated variability observed at other wavelengths. For
 17 1525 sources we have not found plausible counterparts at other wavelengths. More than
 18 2940 of the identified or associated sources are active galaxies of the blazar class, 241
 19 are pulsars.

20 *Keywords:* Gamma rays: general — surveys — catalogs

21 1. INTRODUCTION

22 This document presents the fourth catalog of high-energy γ -ray sources (4FGL) detected in the
 23 first eight years of the *Fermi* Gamma-ray Space Telescope mission by the Large Area Telescope
 24 (LAT). The list is final and this version contains all the source information usually released in Fermi
 25 catalogs except for the spectral energy distributions in broad bins, the light curves and several flags.
 26 A detailed comparison with previous *Fermi*-LAT catalogs and the careful assessment of c sources are
 27 also deferred to a future release. As in the Third LAT Source Catalog (hereafter 3FGL, [Acero et al.](#)
 28 [2015](#)) sources are included based on the statistical significance of their detection considered over the
 29 entire time period of the analysis. For this reason the 4FGL catalog does not contain transient γ -ray
 30 sources which are significant over a short duration (such as γ -ray bursts, solar flares, most novae).

31 The 4FGL catalog builds on several generations of *Fermi*-LAT catalogs (Table 1). It benefits from
 32 a number of improvements with respect to 3FGL, besides the twice longer exposure:

- 33 1. Pass 8 data¹ were used (§ 2.2). The principal difference relative to the P7REP data used for
 34 3FGL is about 20% larger acceptance at all energies and improved angular resolution above 3
 35 GeV.
- 36 2. A new model of underlying diffuse Galactic emission (§ 2.4) was developed.

^a) See <https://fermi.gsfc.nasa.gov/ssc/data/access/lat/fl8y/>.

¹ See http://fermi.gsfc.nasa.gov/ssc/data/analysis/documentation/Pass8_usage.html.

Acronym	Data/IRF/Diffuse model	Energy range/Duration	Sources	Analysis/Reference
1FGL	P6_V3_DIFFUSE gll_iem_v02	0.1 – 100 GeV 11 months	1451 point	Unbinned, F/B Abdo et al. (2010a)
2FGL	P7SOURCE_V6 gal_2yearp7v6_v0	0.1 – 100 GeV 2 years	1873 point	Binned, F/B Nolan et al. (2012)
3FGL	P7REP_SOURCE_V15 gll_iem_v06	0.1 – 300 GeV 4 years	3033 point	Binned, F/B Acero et al. (2015)
FGES	P8R2_SOURCE_V6 gll_iem_v06	10 GeV – 2 TeV 6 years	46 extended	Binned, PSF, $ b < 7^\circ$ Ackermann et al. (2017)
3FHL	P8R2_SOURCE_V6 gll_iem_v06	10 GeV – 2 TeV 7 years	1556 point	Unbinned, PSF Ajello et al. (2017)
FHES	P8R2_SOURCE_V6 gll_iem_v06	1 GeV – 1 TeV 7.5 years	24 extended	Binned, PSF, $ b > 5^\circ$ Ackermann et al. (2018)
4FGL	P8R3_SOURCE_V2 new (§ 2.4.1)	0.05 GeV – 1 TeV 8 years	5098 point	Binned, PSF this work

Table 1. The table describes the previous *Fermi*-LAT catalogs mentioned in the text. In the Analysis column, F/B stands for *Front/Back*, PSF for PSF event types^a. In the Sources column, point or extended refer to the catalog’s objective.

^aSee https://fermi.gsfc.nasa.gov/ssc/data/analysis/LAT_essentials.html.

- 37 3. We introduced weights in the maximum likelihood analysis (§ 3.2) in order to mitigate the
38 effect of systematic errors due to our imperfect knowledge of the Galactic diffuse emission.
- 39 4. We explicitly modeled 75 sources as extended emission regions (§ 3.4), up from 25 in 3FGL.
- 40 5. To study the associations of LAT sources with counterparts at other wavelengths, we updated
41 several of the counterpart catalogs, and correspondingly recalibrated the association procedure.

42 Section 2 describes the LAT, the data and the models for the diffuse backgrounds, celestial and
43 otherwise. Section 3 describes how the catalog is constructed, with emphasis on what has changed
44 since the analysis for the 3FGL catalog. Section 4 describes the catalog itself, while § 5 details the
45 associations and identifications. We provide appendices with technical details of the analysis and of
46 the format of the electronic version of the catalog.

47 2. INSTRUMENT & BACKGROUND

48 2.1. *The Large Area Telescope*

49 The LAT detects γ rays in the energy range 20 MeV to more than 1 TeV, measuring their arrival
50 times, energies, and directions. The field of view of the LAT is 2.4 sr at 1 GeV. The per-photon angular
51 resolution (point-spread function, PSF, 68% containment radius) is $\sim 5^\circ$ at 100 MeV, decreasing to
52 0.8° at 1 GeV (averaged over the acceptance of the LAT), varying with energy approximately as $E^{-0.8}$
53 and asymptoting at $\sim 0.1^\circ$ above 20 GeV². The tracking section of the LAT has 36 layers of silicon
54 strip detectors interleaved with 16 layers of tungsten foil (12 thin layers, 0.03 radiation length, at

² See http://www.slac.stanford.edu/exp/glast/groups/canda/lat_Performance.htm.

55 the top or *Front* of the instrument, followed by 4 thick layers, 0.18 radiation lengths, in the *Back*
 56 section). The silicon strips track charged particles, and the tungsten foils facilitate conversion of γ
 57 rays to positron-electron pairs. Beneath the tracker is a calorimeter composed of an 8-layer array of
 58 CsI crystals (~ 8.5 total radiation lengths) to determine the γ -ray energy. More information about
 59 the LAT is provided in [Atwood et al. \(2009\)](#), and the in-flight calibration of the LAT is described in
 60 [Abdo et al. \(2009a\)](#), [Ackermann et al. \(2012a\)](#) and [Ackermann et al. \(2012b\)](#).

61 The LAT is also an efficient detector of the intense background of charged particles from cosmic
 62 rays and trapped radiation at the orbit of the *Fermi* satellite. A segmented charged-particle
 63 anticoincidence detector (plastic scintillators read out by photomultiplier tubes) around the tracker
 64 is used to reject charged-particle background events. Accounting for γ rays lost in filtering charged
 65 particles from the data, the effective collecting area is ~ 8000 cm² at 1 GeV at normal incidence (for
 66 the P8R3_SOURCE_V2 event selection used here; see below). The live time is nearly 76%, limited
 67 primarily by interruptions of data taking when *Fermi* is passing through the South Atlantic Anomaly
 68 ($\sim 15\%$) and readout dead-time fraction ($\sim 9\%$).

69 2.2. The LAT Data

70 The data for the 4FGL catalog were taken during the period 2008 August 4 (15:43 UTC) to 2016
 71 August 2 (05:44 UTC) covering eight years. As for 3FGL, intervals around solar flares and bright
 72 GRBs were excised. Overall about two days were excised due to solar flares, and 39 ks due to 30
 73 GRBs. The precise time intervals corresponding to selected events are recorded in the GTI extension
 74 of the FITS file (Appendix B). The maximum exposure (4.5×10^{11} cm² s at 1 GeV) is reached at the
 75 North celestial pole. The minimum exposure (2.7×10^{11} cm² s at 1 GeV) is reached at the celestial
 76 equator.

77 The current version of the LAT data is Pass 8 P8R3 ([Atwood et al. 2013](#); [Bruehl et al. 2018](#)). It
 78 offers 20% more acceptance than P7REP ([Bregeson et al. 2013](#)) and a narrower PSF at high energies.
 79 Both aspects are very useful for source detection and localization ([Ajello et al. 2017](#)). We used the
 80 Source class event selection, with the Instrument Response Function (IRF) P8R3_SOURCE_V2.
 81 We took advantage of the new PSF event types, which avoid mixing poorly localized events (PSF0)
 82 with high-quality ones (PSF3).

83 The lower bound of the energy range was set to 50 MeV, down from 100 MeV in 3FGL, in order to
 84 constrain the spectra better at low energy. It does not help detecting or localizing sources because of
 85 the very broad PSF below 100 MeV. The upper bound was raised from 300 GeV in 3FGL to 1 TeV.
 86 This is because as the source-to-background ratio decreases, the sensitivity curve (Figure 18 of [Abdo](#)
 87 [et al. 2010a](#), 1FGL) shifts to higher energies. The 3FHL catalog ([Ajello et al. 2017](#)) went up to 2 TeV,
 88 but only 566 events exceed 1 TeV over 8 years (to be compared to 714 thousands above 10 GeV).

89 2.3. Zenith angle selection

90 The zenith angle cut was set such that the contribution of the Earth limb at that zenith angle was
 91 less than 10% of the total background. Integrated over all zenith angles, the residual Earth limb
 92 contamination is less than 1%. We kept PSF3 event types with zenith angles less than 80° between
 93 50 and 100 MeV, PSF2 and PSF3 event types with zenith angles less than 90° between 100 and
 94 300 MeV, and PSF1, PSF2 and PSF3 event types with zenith angles less than 100° between 300 MeV
 95 and 1 GeV. Above 1 GeV we kept all events with zenith angles less than 105° (Table 2).

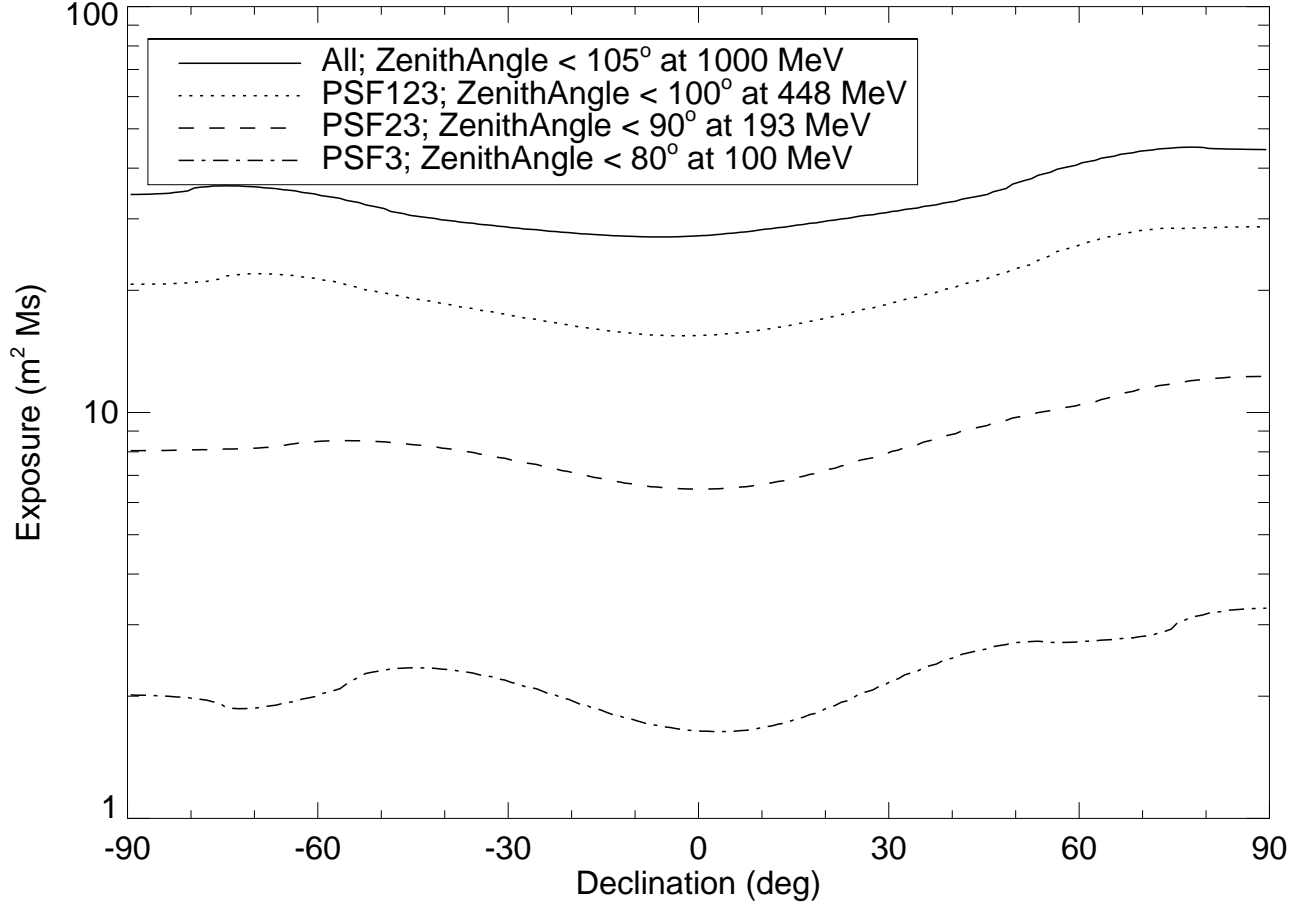


Figure 1. Exposure as a function of declination and energy, averaged over right ascension, summed over all relevant event types as indicated in the figure legend.

Energy interval (GeV)	NBins	ZMax (deg)	Ring width (deg)	Pixel size (deg)				
				PSF0	PSF1	PSF2	PSF3	All
0.05 – 0.1	3	80	7	0.6	
0.1 – 0.3	5	90	7	0.6	0.6	
0.3 – 1	6	100	5	...	0.4	0.3	0.2	
1 – 3	5	105	4	0.4	0.15	0.1	0.1	
3 – 10	6	105	3	0.25	0.1	0.05	0.04	
10 – 1000	10	105	2	0.04

Table 2. The 15 components (all in binned mode) of the Summed Likelihood approach used in 4FGL. Components in a given energy interval share the same number of energy bins, the same zenith angle selection and the same RoI size, but have different pixel sizes in order to adapt to the PSF width. Each filled entry under Pixel size corresponds to one component of the summed likelihood. NBins is the number of energy bins in the interval, ZMax is the zenith angle cut, Ring width refers to the difference between the RoI core and the extraction region, as explained in item 5 of § 3.2.

96 The resulting integrated exposure over 8 years is shown on Figure 1. The dependence on declination
 97 is due to the combination of the inclination of the orbit, the rocking angle and the off-axis effective
 98 area. The north-south asymmetry is due to the south-Atlantic anomaly over which the instrument
 99 is switched off. Because of the regular precession of the orbit every 53 days, the dependence on right
 100 ascension is small when averaged over long periods of time. The dependence on energy is due to the
 101 increase of the effective area up to 1 GeV, and the addition of new event types at 100 MeV, 300 MeV
 102 and 1 GeV. The off-axis effective area depends somewhat on energy and event type. This introduces
 103 a slight dependence of the shape of the curve on energy.

104 Selecting on zenith angle applies a kind of time selection (which depends on direction in the sky).
 105 This means that the effective time selection at low energy is not exactly the same as at high energy.
 106 The periods of time during which a source is at zenith angle $< 105^\circ$ but (for example) $> 90^\circ$
 107 last typically a few minutes every orbit. This is shorter than the main variability time scales of
 108 astrophysical sources, and therefore not a concern. There remains however the modulation due to
 109 the precession of the spacecraft orbit on longer time scales over which blazars can vary. This is not
 110 a problem for a catalog (it can at most appear as a spectral effect, and should average out when
 111 considering statistical properties) but it should be kept in mind when extracting spectral parameters
 112 of individual variable sources. We used the same zenith angle cut for all event types in a given energy
 113 interval in order to reduce systematics due to that time selection.

114 Because the data are limited by systematics at low energies everywhere in the sky (Appendix A)
 115 rejecting half of the events below 300 MeV and 75% of them below 100 MeV does not impact the
 116 sensitivity (if we had kept these events, the weights would have been lower).

117 2.4. Model for the Diffuse Gamma-Ray Background

118 2.4.1. Diffuse emission of the Milky Way

119 We extensively updated the model for Galactic diffuse emission for the 4FGL analysis, using the
 120 same **P8R3** data selections (PSF types, energy ranges, and zenith angle limits). The development
 121 of the model will be described in detail elsewhere. Here we summarize the primary differences from
 122 the model **developed** for the 3FGL catalog (Acero et al. 2016a). In both cases, the model is based
 123 on linear combinations of templates representing components of the Galactic diffuse emission. For
 124 4FGL we updated all of the templates, and added a new one as described below.

125 We have adopted the new, all-sky high-resolution, 21-cm spectral line HI4PI survey (HI4PI
 126 Collaboration et al. 2016) as our tracer of H I, and extensively refined the procedure for partitioning
 127 the H I and H₂ (traced by the 2.6-mm CO line) into separate ranges of Galactocentric distance
 128 (‘rings’), by decomposing the spectra into individual line profiles, so the broad velocity dispersion of
 129 a massive interstellar clouds does not effectively distribute its emission very broadly along the line of
 130 sight. We also updated the rotation curve, and adopted a new procedure for interpolating the rings
 131 across the Galactic center and anticenter, now incorporating a general model for the surface density
 132 distribution of the interstellar medium to inform the interpolation, and defining separate rings for the
 133 Central Molecular Zone (within ~ 150 pc of the Galactic center **and between 150 pc and 600 pc**
 134 **of the center**). With this approach, the Galaxy is divided into ten concentric rings.

135 The template for the inverse Compton emission is still based on a model interstellar radiation field
 136 and cosmic-ray electron distribution (calculated in GALPROP v56, described in Porter et al. 2017)³
 137 but now we formally subdivide the model into rings (with the same Galactocentric radius ranges as
 138 for the gas templates), which are fit separately in the analysis, to allow some spatial freedom relative
 139 to the static all-sky inverse-Compton model.

140 We have also updated the template of the ‘dark gas’ component, representing interstellar gas that
 141 is not traced by the HI and CO line surveys, by comparison with the Planck dust optical depth
 142 map⁴. The dark gas is inferred as the residual component after the best-fitting linear combination
 143 of total $N(\text{HI})$ and W_{CO} are subtracted, i.e., as the component not correlated with the atomic and
 144 molecular gas spectral line tracers, in a procedure similar to that used in Acero et al. (2016a). In
 145 particular, as before we retained the negative residuals as a ‘column density correction map’.

146 New with the 4FGL model we incorporated a template representing the contribution of unresolved
 147 Galactic sources, derived based on a model spatial distribution and luminosity function developed
 148 based on the distribution of Galactic sources in Acero et al. (2015) and an analytical evaluation of
 149 the flux limit for source detection as a function of direction on the sky.

150 As for the 3FGL-era model, we iteratively determined and re-fit a model component that represents
 151 non-template diffuse γ -ray emission, primarily Loop I and the *Fermi* bubbles. To avoid overfitting
 152 the residuals, and possibly suppressing faint Galactic sources, we spectrally and spatially smoothed
 153 the residual template.

154 The model fitting was performed using Gardian, as a summed likelihood analysis. This procedure
 155 involves transforming the ring maps described above into spatial-spectral templates evaluated in
 156 GALPROP. We used a model from Ackermann et al. (2012c), $^S\text{L}^Z\text{G}^R\text{30}^T\text{150}^C\text{2}$. The model is a
 157 linear combination of these templates, with free scaling functions of various forms for the individual
 158 templates. For components with the largest contributions, a piecewise continuous function, linear in
 159 the logarithm of energy, with nine degrees of freedom was used. Other components had a similar
 160 scaling function with five degrees of freedom, or power-law scaling, or overall scale factors, chosen
 161 to give the model adequate freedom while reducing the overall number of free parameters. The
 162 model also required a template for the point and small-extended sources in the sky. We iterated
 163 the fitting using preliminary versions of the 4FGL catalog. This template was also given spectral
 164 degrees of freedom. Other diffuse templates, described below and not related to Galactic emission,
 165 were included in the model fitting.

166 2.4.2. *Isotropic background*

167 The isotropic diffuse background was derived from all-sky fits of the eight-year data set using the
 168 Galactic diffuse emission model described above and a preliminary version of the 4FGL catalog. The
 169 diffuse background includes charged particles misclassified as γ rays. We implicitly assume that the
 170 acceptance for these residual charged particles is the same as for γ rays in treating these diffuse
 171 background components together. For the analysis we derived the contributions to the isotropic
 172 background separately for all event types.

173 2.4.3. *Solar and lunar template*

³ <http://galprop.stanford.edu>

⁴ COM_CompMap_Dust-GNILC-Model-Opacity_2048_R2.01.fits, Planck Collaboration et al. (2016)

174 The quiescent Sun and the Moon are fairly bright γ -ray sources. The Sun moves in the ecliptic but
 175 the solar γ -ray emission is extended because of cosmic-ray interactions with the solar radiation field;
 176 detectable emission from inverse Compton scattering of cosmic-ray electrons on the radiation field
 177 of the Sun extends several degrees from the Sun (Abdo et al. 2011). The Moon is not an extended
 178 source in this way but the lunar orbit is inclined somewhat relative to the ecliptic and the Moon
 179 moves through a larger fraction of the sky than the Sun. Averaged over time, the γ -ray emission
 180 from the Sun and Moon trace a region around the ecliptic. Without any correction this can seriously
 181 affect the spectra and light curves, so starting with 3FGL we model that emission.

182 The Sun and Moon emission are modulated by the solar magnetic field which deflects cosmic rays
 183 more (and therefore reduces γ -ray emission) when the Sun is at maximum activity. For that reason
 184 the model used in 3FGL (based on the first 18 months of data when the Sun was near minimum) was
 185 not adequate for 8 years. We used the improved model of the Moon (Ackermann et al. 2016a) and
 186 a data-based model of the solar disk and inverse Compton scattering on the solar light (S. Raino,
 187 private communication).

188 We combined those models with calculations of their motions and of the exposure of the observations
 189 by the LAT to make templates for the equivalent diffuse component over 8 years using *gtsuntemp*
 190 (Johannesson et al. 2013). For 4FGL we used two different templates: one for the inverse Compton
 191 emission on the solar light (pixel size $0^\circ 25'$) and one for the sum of the solar and lunar disks. For the
 192 latter we reduced the pixel size to $0^\circ 125'$ in order to describe the disks accurately, and computed a
 193 specific template for each event type / maximum zenith angle combination of Table 2 (because their
 194 exposure maps are not identical). As for 3FGL those components have no free parameter.

195 2.4.4. Residual Earth limb template

196 For 3FGL we reduced the low-energy Earth limb emission by selecting zenith angles less than 100° ,
 197 and modeled the residual contamination approximately. For 4FGL we chose to cut harder on zenith
 198 angle at low energies and select event types with the best PSF (§ 2.3). That procedure eliminates
 199 the need for a specific Earth limb component in the model.

200 3. CONSTRUCTION OF THE CATALOG

201 The procedure used to construct the 4FGL catalog has a number of improvements relative to that
 202 of the 3FGL catalog. In this section we review the procedure, emphasizing what was done differently.
 203 The significances (§ 3.2) and spectral parameters (§ 3.3) of all catalog sources were obtained using
 204 the standard *pyLikelihood* framework (Python analog of *gtlike*) in the LAT Science Tools⁵ (version
 205 v11r7p0). The localization procedure (§ 3.1), which relies on *pointlike*, provided the source positions,
 206 the starting point for the spectral fitting, and a comparison for estimating the reliability of the results
 207 (§ 3.5.2).

208 Throughout the text we denote as RoIs, for Regions of Interest, the regions in which we extract
 209 the data. We use the Test Statistic $TS = 2(\log \mathcal{L} - \log \mathcal{L}_0)$ (Mattox et al. 1996) to quantify how
 210 significantly a source emerges from the background, comparing the maximum value of the likelihood
 211 function \mathcal{L} over the RoI including the source in the model with \mathcal{L}_0 , the value without the source.

212 3.1. Detection and Localization

⁵ See <http://fermi.gsfc.nasa.gov/ssc/data/analysis/documentation/Cicerone/>.

213 This section describes the generation of a list of candidate sources, with locations and initial spectral
 214 fits. This initial stage uses *pointlike* (Kerr 2010). Compared with the *gtlike*-based analysis described
 215 in § 3.2 to 3.5, it uses the same time range and IRFs, but the partitioning of the sky, the weights,
 216 the computation of the likelihood function and its optimization are independent. Energy dispersion
 217 is neglected. Events below 100 MeV are useless for source detection and localization, and are ignored
 218 at this stage. Since this version of the computation of the likelihood function is used for localization,
 219 it needs to represent a valid estimate of the probability of observing a point source with the assumed
 220 spectral function.

221 The process started with an initial set of sources from the 3FGL analysis, not just those reported in
 222 that catalog, but also including all candidates failing the significance threshold (i.e., with $10 < TS <$
 223 25). It used the 75 spatially extended sources listed in § 3.4, and the three-source representation
 224 of the Crab (§ 3.3). The same spectral models were considered for each source as in § 3.3, but the
 225 favored model (power law or curved) was not necessarily the same.

226 The generation of a candidate list of sources, with locations and initial spectral fits is substantially
 227 the same as for 3FGL. The sky was partitioned using HEALPix⁶ (Górski et al. 2005) with $N_{\text{side}} = 12$,
 228 resulting in 1728 tiles of ~ 25 deg² area. The RoIs included events in cones of 5° radius about the
 229 center of the tiles. The data were binned into 16 energy bands from 100 MeV to 1 TeV (up from
 230 14 bands to 316 GeV in 3FGL), and, as before, separated into the *Front* and *Back* event types.
 231 However, only *Front* events were used below 316 MeV, to avoid the poor PSF and contribution of
 232 the Earth limb. All sources within the tile and those nearby, in the adjacent and second rings, were
 233 included in the model. Only the spectral models and positions of sources within the central tile were
 234 allowed to vary to optimize the likelihood. To account for correlations with fixed nearby sources,
 235 and a factor of three overlap for the data, iterations were performed until log likelihoods for all RoIs
 236 changed by less than 10.

237 We assumed here that the isotropic spectrum was exactly constant over the sky, but readjusted the
 238 Galactic diffuse emission. Starting with a version of the Galactic diffuse model (§ 2.4.1) without its
 239 non-template diffuse γ -ray emission, we derived an alternative adjustment by optimizing the Galactic
 240 diffuse normalization for each RoI and the eight bands below 10 GeV. These numbers were turned into
 241 an 8-layer map which was smoothed, then applied to the diffuse model itself. Then the corrections
 242 were measured again. This process converged after two iterations, such that no more corrections
 243 were needed. The advantage of the procedure, compared to fitting parameters in each RoI (§ 3.2), is
 244 that the effective predictions do not vary abruptly from an RoI to its neighbors.

245 After a set of iterations had converged, the localization procedure was applied, and source positions
 246 updated for a new set of iterations. At this stage, new sources were occasionally added using the
 247 residual *TS* procedure described below. The detection and localization process resulted in ~ 8020
 248 candidate point sources with $TS > 10$. The fit validation and likelihood weighting were done as in
 249 3FGL.

250 3.1.1. Detection of additional sources

251 As for 3FGL, the same implementation of the likelihood used for optimizing source parameters was
 252 used to test for the presence of additional point sources. This is inherently iterative, in that the
 253 likelihood is valid to the extent that it represents an accurate measure of the model prediction. Thus

⁶ <http://healpix.sourceforge.net>.

α	β	E_0 (GeV)	Comment
1.7	0.0	50.00	Hard
2.2	0.0	1.00	Intermediate
2.7	0.0	0.25	Soft
2.0	0.5	2.00	Curved, but not a pulsar
2.0	0.3	1.00	Pulsar-like

Table 3. The table describes the five spectral shapes used for source finding in 4FGL. The spectral parameters α , β and E_0 refer to the LogParabola spectral shape (Eq. 2).

254 source detection depends on having nearby stronger sources already included. Since 3FGL was based
 255 on four years of data, one can expect many more sources. As we accumulated more and more data
 256 since then, the source list gradually evolved. A measure of success is that subsequent source finding
 257 adds little to the total. As before, an iteration starts with choosing a HEALPix $N_{side} = 128$ grid,
 258 3.1 M points with average separation 0.15 degrees. But now, instead of testing a single power-law
 259 spectrum, we try five spectral shapes; three are power laws with different indices, two with significant
 260 curvature. Table 3 lists the spectral shapes used for the templates.

261 For each trial position, and each of the five templates, the normalizations were optimized, and
 262 the resulting TS associated with the pixel. Then, as before, but independently for each template, a
 263 cluster analysis selected groups of pixels with $TS > 16$, as compared to $TS > 10$ for 3FGL. Each
 264 cluster defined a seed, with a position defined by weighting the TS values. Finally, the five sets of
 265 potential seeds were compared, and, for those within 1° , the seed with the largest TS was selected
 266 for inclusion.

267 3.1.2. Localization

268 The position of each source was determined by maximizing the likelihood with respect to its position
 269 only. That is, all other parameters are kept fixed. The possibility that a shifted position would affect
 270 the spectral models or positions of nearby sources is accounted for by iteration. Ideally the log
 271 likelihood is a quadratic form in any pair of angular variables, assuming small angular offsets. We
 272 define LTS, for Localization Test Statistic, to be twice the log of the likelihood ratio of any position
 273 with respect to the maximum; the LTS evaluated for a grid of positions is called an LTS map. We fit
 274 the distribution of LTS to a quadratic form to determine the uncertainty ellipse, the major and minor
 275 axes and orientation. We also define a measure, the localization quality (LQ), of how well the actual
 276 LTS distribution matches this expectation by reporting the sum of the squares of the deviations of
 277 eight points evaluated from the fit at a circle of radius corresponding to twice the geometric mean of
 278 the two Gaussian sigmas.

279 We flagged apparently significant sources that do not have good localization fits ($LQ > 8$) with Flag
 280 9 (Table 5) and for them estimated the position and uncertainty by performing a moment analysis of
 281 the LTS function instead of fitting a quadratic form. Some sources that did not have a well-defined
 282 peak in the likelihood were discarded by hand, on the consideration that they were most likely related
 283 to residual diffuse emission. Another possibility is that two adjacent sources produce a dumbbell-like
 284 shape; for a few of these cases we added a new source by hand.

285 As in 3FGL, we checked the brightest sources spatially associated with likely multiwavelength
 286 counterparts, comparing their localizations with the well-measured positions of the counterparts. The

287 smaller statistical source localization errors in 4FGL allowed us to estimate the absolute precision Δ_{abs}
 288 (at the 95% confidence level) more accurately to $\sim 0^{\circ}.0075$, up from $\sim 0^{\circ}.005$ in 3FGL. The systematic
 289 factor f_{rel} was the same 1.05 as in 3FGL. Eq. 1 shows how the statistical errors Δ_{stat} are transformed
 290 into total errors Δ_{tot} :

$$\Delta_{\text{tot}}^2 = (f_{\text{rel}} \Delta_{\text{stat}})^2 + \Delta_{\text{abs}}^2 \quad (1)$$

291 applies to the two ellipse axes separately.

3.2. Significance and Thresholding

292
 293 The framework for this stage of the analysis is inherited from the 3FGL catalog. It splits the
 294 sky into RoIs, varying typically half a dozen sources near the center of the RoI at the same time.
 295 There are 1748 RoIs for 4FGL, listed in the ROIs extension of the catalog (Appendix B). The global
 296 best fit is reached iteratively, injecting the spectra of sources in the outer parts of the RoI from the
 297 previous step or iteration. In this approach the diffuse emission model (§ 2.4) is taken from the global
 298 templates (including the spectrum, unlike what is done with *pointlike* in § 3.1) but it is modulated
 299 in each RoI by three parameters: normalization (at 1 GeV) and small corrective slope of the Galactic
 300 component and normalization of the isotropic component.

301 Among more than 8,000 seeds coming from the localization stage, we keep only sources with $TS >$
 302 25, corresponding to a significance of just over 4σ evaluated from the χ^2 distribution with 4 degrees
 303 of freedom (position and spectral parameters of a power-law source, [Mattox et al. 1996](#)). The model
 304 for the current RoI is readjusted after removing each seed below threshold, so that the final model fits
 305 the full data. The low-energy flux of the seeds below threshold (a fraction of which are real sources)
 306 can be absorbed by neighboring sources closer than the PSF radius.

307 As in 3FGL we manually added known LAT pulsars that could not be localized by the automatic
 308 procedure without phase selection. However none of those reached $TS > 25$ in 4FGL.

309 We introduced a number of improvements with respect to 3FGL (by decreasing order of
 310 importance):

- 311 1. In 3FGL we had already noted that systematic errors due to an imperfect modeling of diffuse
 312 emission were larger than statistical errors in the Galactic plane, and at the same level over
 313 the entire sky. With twice as much exposure and an improved effective area at low energy
 314 with Pass 8, the effect now dominates. The approach adopted in 3FGL (comparing runs
 315 with different diffuse models) allowed characterizing the effect globally and flagging the worst
 316 offenders, but left purely statistical errors on source parameters. In 4FGL we introduce weights
 317 in the maximum likelihood approach (Appendix A). This allows obtaining directly (although in
 318 an approximate way) smaller TS and larger parameter errors, reflecting the level of systematic
 319 uncertainties. We estimated the relative spatial and spectral residuals in the Galactic plane
 320 where the diffuse emission is strongest. The resulting systematic level $\epsilon \sim 3\%$ was used to
 321 compute the weights. This is by far the most important improvement, which avoids reporting
 322 many dubious soft sources.
- 323 2. The automatic iteration procedure at the next-to-last step of the process was improved. There
 324 are now two iteration levels. In a standard iteration the sources and source models are fixed
 325 and only the parameters are free. An RoI and all its neighbors are run again until $\log \mathcal{L}$ does
 326 not change by more than 10 from the previous iteration. Around that we introduce another

iteration level (superiterations). At the first iteration of a given superiteration we reenter all seeds and remove (one by one) those with $TS < 16$. We also systematically check curvature significance (§ 3.3) at this first iteration, and allow sources to switch to a curved spectral shape if $TS_{\text{curv}} > 9$ or force them back to power law if $TS_{\text{curv}} < 9$ (§ 3.3). At the end of a superiteration an RoI (and its neighbors) enters the next superiteration until $\log \mathcal{L}$ does not change by more than 10 from the last iteration of the previous superiteration. This procedure stabilizes the spectral shapes, particularly in the Galactic plane. Seven superiterations were required to reach full convergence.

3. The fits are now performed from 50 MeV to 1 TeV, and the overall significances (`Signif_Avg`) as well as the spectral parameters refer to the full band. The total energy flux, on the other hand, is still reported between 100 MeV and 100 GeV. For hard sources with photon index less than 2 integrating up to 1 TeV would result in much larger uncertainties. The same is true for soft sources with photon index larger than 2.5 when integrating down to 50 MeV.
4. We considered the effect of energy dispersion, in the approximate way implemented in the Science Tools. The effect of energy dispersion is calculated globally for each source, and applied to the whole 3D model of that source, rather than accounting for energy dispersion separately in each pixel. This approximate rescaling captures the main effect at a very minor computational cost. The effect of energy dispersion on the spectra is relatively small. It tends to increase the energy flux (by 4% on average), to reduce the width of the power-law index distribution (by making hard sources softer and soft sources harder, but changing the index by less than 0.02), and to make spectra more curved (because energy dispersion acts as a convolution) but increasing β by only 0.01 on average. In evaluating the likelihood function the effects of energy dispersion were not applied to the isotropic background and the Sun/Moon components whose spectra were obtained from the data without considering energy dispersion.
5. We used smaller RoIs at higher energy because we are interested in the core region only, which contains the sources whose parameters come from that RoI (sources in the outer parts of the RoI are entered only as background). The core region is the same for all energy intervals, and the RoI is obtained by adding a ring to that core region, whose width adapts to the PSF and therefore decreases with energy (Table 2). This does not affect the result because the outer parts of the RoI would not have been correlated to the inner sources at high energy anyway, but saves memory and CPU time.
6. At the last step of the fitting procedure we tested all spectral shapes described in § 3.3 (including log-normal for pulsars and cutoff power law for other sources), readjusting the parameters (but not the spectral shapes) of neighboring sources.

We used only binned likelihood analysis in 4FGL because unbinned mode is much more CPU intensive, and does not support weights or energy dispersion. We split the data into fifteen components, selected according to PSF event type and described in Table 2. As explained in § 2.4.4 at low energy we kept only the event types with the best PSF. Each event type selection has its own isotropic diffuse template (because it includes residual charged-particle background, which depends on event type). A single component is used above 10 GeV in order to save memory and CPU time:

at high energy the background under the PSF is small, so keeping the event types separate does not improve significance very much; it would help for localization, but this is done separately (§ 3.1.2).

A known inconsistency in acceptance exists between Pass 8 PSF event types. It is easy to see on bright sources or the entire RoI spectrum and peaks at the level of 10% between PSF0 (positive residuals, underestimated effective area) and PSF3 (negative residuals, overestimated effective area) at a few GeV. In that range all event types were considered so the effect on source spectra should be minor. Below 1 GeV the PSF0 event type was discarded so the inconsistency could introduce a downward bias (appearing as slightly too hard spectra) but the discrepancy is lower at low energy. The bias on power-law index is estimated to be ~ -0.01 .

3.3. Spectral Shapes

The spectral representation of sources largely follows what was done in 3FGL, considering three spectral models (power law, power law with subexponential cutoff, log-normal). We changed two important things in the way we parametrize the cutoff power law:

- The cutoff energy was replaced by an exponential factor (a in Eq. 3) which is allowed to be positive. This makes the simple power law a special case of the cutoff power law and allows fitting that model to all sources.
- We set the exponential index (b in Eq. 3) to $2/3$ (instead of 1) for all pulsars that are too faint for it to be left free. This recognizes the fact that $b < 1$ (subexponential) in all bright pulsars. Among the six brightest pulsars, three have $b \sim 0.55$ and three have $b \sim 0.75$). We chose $2/3$ as a simple intermediate value.

Therefore the spectral representations which can be found in 4FGL are:

- a log-normal representation (`LogParabola` in the tables) for all significantly curved spectra except pulsars, 3C 454.3 and the Small Magellanic Cloud (SMC):

$$\frac{dN}{dE} = K \left(\frac{E}{E_0} \right)^{-\alpha - \beta \log(E/E_0)} \quad (2)$$

where \log is the natural logarithm. The reference energy E_0 is set to `Pivot_Energy` in the tables. The parameters K , α (spectral slope at E_0) and the curvature β appear as `LP_Flux_Density`, `LP_Index` and `LP_beta` in the tables, respectively. No significantly negative β (spectrum curved upwards) was found. The maximum allowed β was set to 1 as in 3FGL.

- a subexponentially cutoff power law for all significantly curved pulsars (`PLSuperExpCutoff` in the tables):

$$\frac{dN}{dE} = K \left(\frac{E}{E_0} \right)^{-\Gamma} \exp(a(E_0^b - E^b)) \quad (3)$$

where E_0 and E in the exponential are expressed in MeV. The reference energy E_0 is set to `Pivot_Energy` in the tables and the parameters K , Γ (low-energy spectral slope), a (exponential factor in MeV^{-b}) and b (exponential index) appear as `PLEC_Flux_Density`, `PLEC_Index`, `PLEC_Expfactor` and `PLEC_Exp_Index` in the tables, respectively. Note that in the Science Tools that spectral shape is called `PLSuperExpCutoff2` and no E_0^b term appears in the

exponential, so the error on K in the tables was obtained from the covariance matrix. The minimum Γ was set to 0 (in 3FGL it was set to 0.5, but a smaller b results in a smaller Γ). No significantly negative a (spectrum curved upwards) was found.

- a simple power-law form (Eq. 3 without the exponential term) for all sources not significantly curved. For those parameters K and Γ appear as `PL_Flux_Density` and `PL_Index` in the tables.

A source is considered significantly curved if $TS_{\text{curv}} > 9$ (3σ significance) where $TS_{\text{curv}} = 2 \log(\mathcal{L}(\text{curved spectrum})/\mathcal{L}(\text{power-law}))$. When this is achieved the global model (used to fit neighboring sources) uses the curved representation. We used a lower TS_{curv} threshold than in 3FGL (where it was 16, or 4σ) for two reasons. First, all bright sources are actually significantly curved downwards so there is no good reason to penalize the curved models too much. Second, the power-law model tends to exceed the data at both ends of the spectrum, where constraints are weak. It is not a worry at high energy, but at low energy the collection of faint sources modeled as power laws generates an effectively diffuse excess in the model, which will make the curved sources more curved than they should be. Using a `LogParabola` spectral shape for all sources would be even better physically, but the very large correlation between sources at low energy due to the broad PSF makes that unstable. The curvature significance ($\sqrt{TS_{\text{curv}}}$) is reported as `LP_SigCurv` or `PLEC_SigCurv`.

Sources with curved spectra are considered significant whenever $TS > 25 + 9 = 34$. This is conservative enough, and accepts a few more strongly curved faint sources (pulsar-like) than the 3FGL criterion which requested $TS > 25$ in the power-law representation.

One more pulsar (PSR J1057–5226) was fit with a free exponential index, besides the six sources modeled in this way in 3FGL. The Crab was modeled with three spectral components as in 3FGL, but the inverse Compton emission of the nebula was represented as a log-normal law instead of a simple power law. The parameters of that component were fixed to $\alpha = 1.75$, $\beta = 0.08$, $K = 5.5 \times 10^{-13}$ ph/cm²/MeV/s at 10 GeV, mimicking the broken power-law fit by [Buehler et al. \(2012\)](#). They were unstable (too much correlation with the pulsar) without phase selection. Four other sources had fixed parameters in 3FGL. These were freed in 4FGL.

Overall in 4FGL seven sources (the six brightest pulsars and 3C 454.3) were fit as `PLSuperExpCutoff` with free b (Eq. 3), 215 pulsars were fit as `PLSuperExpCutoff` with $b = 2/3$, the SMC was fit as `PLSuperExpCutoff` with $b = 1$, 1332 sources were fit as `LogParabola` (including the fixed inverse Compton component of the Crab and 38 other extended sources) and the rest were represented as power laws. The larger fraction of curved spectra compared to 3FGL is due to the lower TS_{curv} threshold.

The way the parameters are reported has changed as well:

- The spectral shape parameters are now explicitly associated to the spectral model they come from. They are reported as `Shape_Param` where `Shape` is one of `PL` (`PowerLaw`), `PLEC` (`PLSuperExpCutoff`) or `LP` (`LogParabola`) and `Param` is the parameter name. Columns `Shape_Index` replace `Spectral_Index` which was ambiguous.
- All sources were fit with the three spectral shapes, so all fields are filled. The curvature significance is calculated twice by comparing power law with both log-normal and exponentially cutoff power law (although only one is actually used to switch to the curved shape in the

442 global model, depending on whether the source is a pulsar or not). There are also three
 443 `Shape_Flux_Density` columns referring to the same `Pivot_Energy`.

444 This representation allows comparing unassociated sources with either pulsars or blazars using the
 445 same spectral shape. The preferred spectral shape (reported as `SpectrumType`) remains what is used
 446 in the global model, when the source is part of the background (i.e., when fitting the other sources).
 447 It is also what is used to derive the fluxes, their uncertainties and the significance.

448 3.4. *Extended Sources*

449 As for the 3FGL catalog, we explicitly model as spatially extended those LAT sources that have
 450 been shown in dedicated analyses to be resolved by the LAT. The catalog process does not involve
 451 looking for new extended sources, testing possible extension of sources detected as point-like, nor
 452 refitting the spatial shapes of known extended sources.

453 Most templates are geometrical, so they are not perfect matches to the data and the source
 454 detection often finds residuals on top of extended sources, which are then converted into additional
 455 point sources. As in 3FGL those additional point sources were voluntarily deleted from the model,
 456 except if they met two of the following criteria: associated, much harder than the extended source
 457 (`Pivot_Energy` larger by a factor e or more), very significant ($TS > 100$). Contrary to 3FGL, that
 458 procedure was applied inside the Cygnus X cocoon as well.

459 The latest pre-4FGL compilation is the 55 extended sources entered in 3FGL, which includes the
 460 result of the systematic search for new sources in the Galactic plane ($|b| < 7^\circ$) above 10 GeV (FGES,
 461 [Ackermann et al. 2017](#)). Two of those were not propagated to 4FGL:

- 462 • FGES J1800.5–2343 was replaced by the W 28 template from 3FGL, and the nearby excesses
 463 ([Hanabata et al. 2014](#)) were left to be modeled as point sources.
- 464 • FGES J0537.6+2751 was replaced by the radio template of S 147 used in 3FGL, which fits
 465 better than the disk used in the FGES paper (S 147 is a soft source, so it was barely detected
 466 above 10 GeV).

467 MSH 15-56 was replaced by two morphologically distinct components, following [Devin et al. \(2018\)](#):
 468 one for the SNR (SNR mask in the paper), the other one for the PWN inside it (radio template). We
 469 added back the W 30 SNR on top of FGES J1804.7–2144 (coincident with HESS J1804–216). The
 470 two overlap but the best localization clearly moves with energy from W 30 to HESS J1804–216.

471 Eighteen sources were added, resulting in 75 extended sources in 4FGL:

- 472 • The Rosette nebula and Monoceros SNR (too soft to be detected above 10 GeV) were
 473 characterized by [Katagiri et al. \(2016b\)](#). We used the same templates.
- 474 • The systematic search for extended sources outside the Galactic plane above 1 GeV (FHES,
 475 [Ackermann et al. 2018](#)) found sixteen reliable extended sources. Five of them were already
 476 known as extended sources. We ignored two others: M 31 (extension only marginally significant)
 477 and SNR G119.5+10.2 around PSR J0007+7303 (not significant without phase gating). We
 478 introduced the nine remaining FHES sources (including the Crab nebula and the ρ Oph
 479 molecular cloud). One of them (J1741.6-3917) was reported by [Araya \(2018a\)](#) as well, with
 480 similar extension.

- 481 • Four HESS sources were found to be extended sources in the *Fermi* range as well: J1534-571
482 ([Araya 2017](#)), J1808-204 ([Yeung et al. 2016](#)), J1809-193 and J1813-178 ([Araya 2018b](#)).
- 483 • Three extended sources were discovered in the search for GeV emission from magnetars ([Li
484 et al. 2017a](#)). They contain SNRs (Kes 73, Kes 79 and G42.8+0.6 respectively) but are much
485 bigger than the radio SNRs. One of them (around Kes 73) was also noted by [Yeung et al.
486 \(2017\)](#).

487 Table 4 lists the source name, origin, spatial template and the reference for the dedicated analysis.
488 These sources are tabulated with the point sources, with the only distinction being that no position
489 uncertainties are reported and their names end in e (see Appendix B). Unidentified point sources
490 inside extended ones are indicated as “xxx field” in the ASSOC2 column of the catalog.

Table 4. Extended Sources Modeled in the 4FGL Analysis

4FGL Name	Extended Source	Origin	Spatial Form	Extent [deg]	Reference
J0058.0–7245e	SMC Galaxy	Updated	Map	1.5	Caputo et al. (2016)
J0221.4+6241e	HB 3	New	Disk	0.8	Katagiri et al. (2016a)
J0222.4+6156e	W 3	New	Map	0.6	Katagiri et al. (2016a)
J0322.6–3712e	Fornax A	3FHL	Map	0.35	Ackermann et al. (2016c)
J0427.2+5533e	SNR G150.3+4.5	3FHL	Disk	1.515	Ackermann et al. (2017)
J0500.3+4639e	HB 9	New	Map	1.0	Araya (2014)
J0500.9–6945e	LMC FarWest	3FHL	Map ^a	0.9	Ackermann et al. (2016d)
J0519.9–6845e	LMC Galaxy	New	Map ^a	3.0	Ackermann et al. (2016d)
J0530.0–6900e	LMC 30DorWest	3FHL	Map ^a	0.9	Ackermann et al. (2016d)
J0531.8–6639e	LMC North	3FHL	Map ^a	0.6	Ackermann et al. (2016d)
J0534.5+2201e	Crab nebula IC	New	Gaussian	0.03	Ackermann et al. (2018)
J0540.3+2756e	S 147	3FGL	Disk	1.5	Katsuta et al. (2012)
J0617.2+2234e	IC 443	2FGL	Gaussian	0.27	Abdo et al. (2010b)
J0634.2+0436e	Rosette	New	Map	(1.5, 0.875)	Katagiri et al. (2016b)
J0639.4+0655e	Monoceros	New	Gaussian	3.47	Katagiri et al. (2016b)
J0822.1–4253e	Puppis A	3FHL	Disk	0.443	Ackermann et al. (2017)
J0833.1–4511e	Vela X	2FGL	Disk	0.91	Abdo et al. (2010c)
J0851.9–4620e	Vela Junior	3FHL	Disk	0.978	Ackermann et al. (2017)
J1023.3–5747e	Westerlund 2	3FHL	Disk	0.278	Ackermann et al. (2017)
J1036.3–5833e	FGES J1036.3–5833	3FHL	Disk	2.465	Ackermann et al. (2017)
J1109.4–6115e	FGES J1109.4–6115	3FHL	Disk	1.267	Ackermann et al. (2017)
J1208.5–5243e	SNR G296.5+10.0	3FHL	Disk	0.76	Acero et al. (2016b)
J1213.3–6240e	FGES J1213.3–6240	3FHL	Disk	0.332	Ackermann et al. (2017)
J1303.0–6312e	HESS J1303–631	3FGL	Gaussian	0.24	Aharonian et al. (2005)
J1324.0–4330e	Centaurus A (lobes)	2FGL	Map	(2.5, 1.0)	Abdo et al. (2010d)
J1355.1–6420e	HESS J1356–645	3FHL	Disk	0.405	Ackermann et al. (2017)
J1409.1–6121e	FGES J1409.1–6121	3FHL	Disk	0.733	Ackermann et al. (2017)
J1420.3–6046e	HESS J1420–607	3FHL	Disk	0.123	Ackermann et al. (2017)
J1443.0–6227e	RCW 86	3FHL	Map	0.3	Ajello et al. (2016)
J1501.0–6310e	FHES J1501.0–6310	New	Gaussian	1.29	Ackermann et al. (2018)
J1507.9–6228e	HESS J1507–622	3FHL	Disk	0.362	Ackermann et al. (2017)
J1514.2–5909e	MSH 15–52	3FHL	Disk	0.243	Ackermann et al. (2017)
J1533.9-5712e	HESS J1534–571	New	Disk	0.4	Araya (2017)

Table 4 continued on next page

Table 4 (continued)

4FGL Name	Extended Source	Origin	Spatial Form	Extent [deg]	Reference
J1552.4-5612e	MSH 15-56 PWN	New	Map	0.08	Devin et al. (2018)
J1552.9-5607e	MSH 15-56 SNR	New	Map	0.3	Devin et al. (2018)
J1553.8-5325e	FGES J1553.8-5325	3FHL	Disk	0.523	Ackermann et al. (2017)
J1615.3-5146e	HESS J1614-518	3FGL	Disk	0.42	Lande et al. (2012)
J1616.2-5054e	HESS J1616-508	3FGL	Disk	0.32	Lande et al. (2012)
J1626.9-2431e	FHES J1626.9-2431	New	Gaussian	0.29	Ackermann et al. (2018)
J1631.6-4756e	FGES J1631.6-4756	3FHL	Disk	0.256	Ackermann et al. (2017)
J1633.0-4746e	FGES J1633.0-4746	3FHL	Disk	0.61	Ackermann et al. (2017)
J1636.3-4731e	SNR G337.0-0.1	3FHL	Disk	0.139	Ackermann et al. (2017)
J1642.1-5428e	FHES J1642.1-5428	New	Disk	0.696	Ackermann et al. (2018)
J1652.2-4633e	FGES J1652.2-4633	3FHL	Disk	0.718	Ackermann et al. (2017)
J1655.5-4737e	FGES J1655.5-4737	3FHL	Disk	0.334	Ackermann et al. (2017)
J1713.5-3945e	RX J1713.7-3946	3FHL	Map	0.56	H. E. S. S. Collaboration et al. (2018)
J1723.5-0501e	FHES J1723.5-0501	New	Gaussian	0.73	Ackermann et al. (2018)
J1741.6-3917e	FHES J1741.6-3917	New	Disk	1.65	Ackermann et al. (2018)
J1745.8-3028e	FGES J1745.8-3028	3FHL	Disk	0.528	Ackermann et al. (2017)
J1801.3-2326e	W 28	2FGL	Disk	0.39	Abdo et al. (2010e)
J1804.7-2144e	HESS J1804-216	3FHL	Disk	0.378	Ackermann et al. (2017)
J1805.6-2136e	W 30	2FGL	Disk	0.37	Ajello et al. (2012)
J1808.2-2028e	HESS J1808-204	New	Disk	0.65	Yeung et al. (2016)
J1810.3-1925e	HESS J1809-193	New	Disk	0.5	Araya (2018b)
J1813.1-1737e	HESS J1813-178	New	Disk	0.6	Araya (2018b)
J1824.5-1351e	HESS J1825-137	2FGL	Gaussian	0.75	Grondin et al. (2011)
J1834.1-0706e	SNR G24.7+0.6	3FHL	Disk	0.214	Ackermann et al. (2017)
J1834.5-0846e	W 41	3FHL	Gaussian	0.23	Abramowski et al. (2015)
J1836.5-0651e	FGES J1836.5-0651	3FHL	Disk	0.535	Ackermann et al. (2017)
J1838.9-0704e	FGES J1838.9-0704	3FHL	Disk	0.523	Ackermann et al. (2017)
J1840.8-0453e	Kes 73	New	Disk	0.32	Li et al. (2017a)
J1840.9-0532e	HESS J1841-055	3FGL	2D Gaussian	(0.62, 0.38)	Aharonian et al. (2008)
J1852.4+0037e	Kes 79	New	Disk	0.63	Li et al. (2017a)
J1855.9+0121e	W 44	2FGL	2D Ring	(0.30, 0.19)	Abdo et al. (2010f)
J1857.7+0246e	HESS J1857+026	3FHL	Disk	0.613	Ackermann et al. (2017)
J1908.6+0915e	SNR G42.8+0.6	New	Disk	0.6	Li et al. (2017a)
J1923.2+1408e	W 51C	2FGL	2D Disk	(0.375, 0.26)	Abdo et al. (2009b)
J2021.0+4031e	γ -Cygni	3FGL	Disk	0.63	Lande et al. (2012)
J2028.6+4110e	Cygnus X cocoon	3FGL	Gaussian	3.0	Ackermann et al. (2011a)
J2045.2+5026e	HB 21	3FGL	Disk	1.19	Pivato et al. (2013)
J2051.0+3040e	Cygnus Loop	2FGL	Ring	1.65	Katagiri et al. (2011)
J2129.9+5833e	FHES J2129.9+5833	New	Gaussian	1.09	Ackermann et al. (2018)
J2208.4+6443e	FHES J2208.4+6443	New	Gaussian	0.93	Ackermann et al. (2018)
J2301.9+5855e	CTB 109	3FHL	Disk	0.249	Ackermann et al. (2017)
J2304.0+5406e	FHES J2304.0+5406	New	Gaussian	1.58	Ackermann et al. (2018)

^aEmissivity model.

NOTE— List of all sources that have been modeled as spatially extended. The Origin column gives the name of the *Fermi*-LAT catalog in which that spatial template was introduced. The Extent column indicates the radius for Disk (flat disk) sources, the 68% containment radius for Gaussian sources, the outer radius for Ring (flat annulus) sources, and an approximate radius for Map (external template) sources. The 2D shapes are elliptical; each pair of parameters (a, b) represents the semi-major (a) and semi-minor (b) axes.

3.5. *Limitations and Systematic Uncertainties*

3.5.1. *Diffuse emission model*

The model of diffuse emission is the main source of uncertainties for faint sources. Contrary to the effective area, it does not affect all sources equally: its effects are smaller outside the Galactic plane where the diffuse emission is fainter and varying on larger angular scales. It is also less of a concern at high energy (> 3 GeV) where the core of the PSF is narrow enough that the sources dominate the background under the PSF. But it is a serious concern inside the Galactic plane at low energy (< 1 GeV) and particularly inside the Galactic ridge ($|l| < 60^\circ$) where the diffuse emission is strongest and very structured, following the molecular cloud distribution. It is not easy to assess precisely how large the uncertainties are, because they relate to uncertainties in the distributions of interstellar gas, the interstellar radiation field, and cosmic rays, which depend in detail on position on the sky.

We estimate, from the residuals over the entire Galactic plane, that the systematics are at the 3% level. This is already an achievement, but the statistical Poisson errors corresponding to the diffuse emission integrated over the PSF (as described in Appendix A) are much smaller than this. Integrating energies up to twice the current one in the Galactic ridge, the statistical precision is 0.2, 0.4, 1, 2, 5% above 100, 200, 500 MeV, 1, 2 GeV respectively.

The weights are able to mitigate the systematic effects globally, but cannot correct the model locally. In particular underestimating the mass of an interstellar cloud will always tend to create spurious sources on top of it, and overestimating diffuse emission at a particular place tends to make the sources on top of it harder than they should be (because the model creates negative residuals there, and those are felt mostly at low energy).

3.5.2. *Analysis method*

As in 3FGL, we use the *pointlike*-based method described in § 3.1 to estimate systematic errors due to the way the main *gtlike*-based method (§ 3.2) is set up in detail. Many aspects differ between the two methods: the code, the weights implementation, the RoIs, the diffuse model adjustments. The *pointlike*-based method does not remove faint sources (with $TS < 25$) from the model. Even the data differ, since the *pointlike*-based method uses *Front* and *Back* event types whereas the *gtlike*-based method uses PSF event types with a different zenith angle cut. Both methods reject a fraction of the events below 1 GeV, but not the same one.

Because of all those differences, we expect that comparing the results of the two methods source by source can provide an estimate of the sensitivity of the source list to details of the analysis. In particular we use it to flag sources whose spectral characterization differs a lot with the two methods (Flags 1 and 3 in Table 5).

3.5.3. *Analysis Flags*

As in 3FGL we identified a number of conditions that should be considered cautionary regarding the reality of a source or the magnitude of the systematic uncertainties of its measured properties. They are described in Table 5. Because this is a preliminary catalog a number of flags are unfilled (4, 5, 6, 7, 11).

In 4FGL 877 sources are flagged (about 17%): 207 sources were flagged with flag 1, 227 were flagged with flag 2, 333 were flagged with flag 3 (those three flags alert to a different result with *pointlike* or the previous diffuse model), 98 with flag 9 (bad localization), 35 with flag 10 (bad spectral representation) and 154 with flag 12 (highly curved).

Table 5. Definitions of the Analysis Flags

Flag ^a	Meaning
1	Source with $TS > 35$ which went to $TS < 25$ when changing the diffuse model (§ 3.5.1) or the analysis method (§ 3.5.2). Sources with $TS \leq 35$ are not flagged with this bit because normal statistical fluctuations can push them to $TS < 25$.
2	Moved beyond its 95% error ellipse when changing the diffuse model.
3	Flux (> 1 GeV) or energy flux (> 100 MeV) changed by more than 3σ when changing the diffuse model or the analysis method. Requires also that the flux change by more than 35% (to not flag strong sources).
4	Not used.
5	Not used.
6	Not used.
7	Not used.
8	Not used.
9	Localization Quality > 8 in <i>pointlike</i> (§ 3.1) or long axis of 95% ellipse $> 0^\circ.25$.
10	Spectral Fit Quality > 30 in <i>pointlike</i> .
11	Not used.
12	Highly curved spectrum; LP_beta fixed to 1 or PLEC_Index fixed to 0 (see § 3.3).

^aIn the FITS version (Table 9 in Appendix B) the values are encoded as individual bits in a single column, with Flag n having value $2^{(n-1)}$.

533 Only 12% of the sources with power-law index $\Gamma < 2.5$ are flagged, but 34% of the soft sources with
534 $\Gamma \geq 2.5$. This attests of the exacerbated sensitivity of soft sources to the underlying background
535 emission. Only 10% of associated sources are flagged but 24% of the non-associated ones. This is
536 in part because the associated sources tend to be brighter, therefore more robust, and also because
537 many flagged sources are close to the Galactic plane where the association rate is low.

538 4. THE 4FGL CATALOG

539 4.1. Catalog Description

540 The catalog contains 5098 sources⁷. The source designation is 4FGL JHHMM.m+DDMM where the 4
541 indicates that this is the fourth LAT catalog, FGL represents *Fermi* Gamma-ray LAT. The 75 sources
542 that were modeled as extended for 4FGL (§ 3.4) are singled out by an e appended to their names.
543 The catalog columns are described in Appendix B. Figure 2 illustrates the distribution of the 4FGL
544 sources over the sky, separately for extragalactic (blue) and Galactic (red) classes.

545 4.2. Comparison with 3FGL and earlier

546 4.2.1. General comparison

547 Figure 3 shows the energy flux distribution in 1FGL, 2FGL, 3FGL and 4FGL. Comparing the
548 current flux threshold with those published in previous LAT Catalog papers we see that in 4FGL the
549 threshold is down to $\simeq 2 \times 10^{-12}$ erg cm⁻² s⁻¹, quantifying the gain from 3FGL. Above 10^{-11} erg cm⁻²
550 s⁻¹ the 2FGL and 3FGL distributions are entirely compatible with 4FGL. The 1FGL distribution
551 shows a distinct bump between 1 and 2×10^{-11} erg cm⁻² s⁻¹. That accumulation of fluxes was clearly
552 incorrect. We attribute it primarily to overestimating significances and fluxes due to the unbinned

⁷ The file has 5099 entries because the PWN component of the Crab nebula is represented by two cospatial sources (§ 3.3).

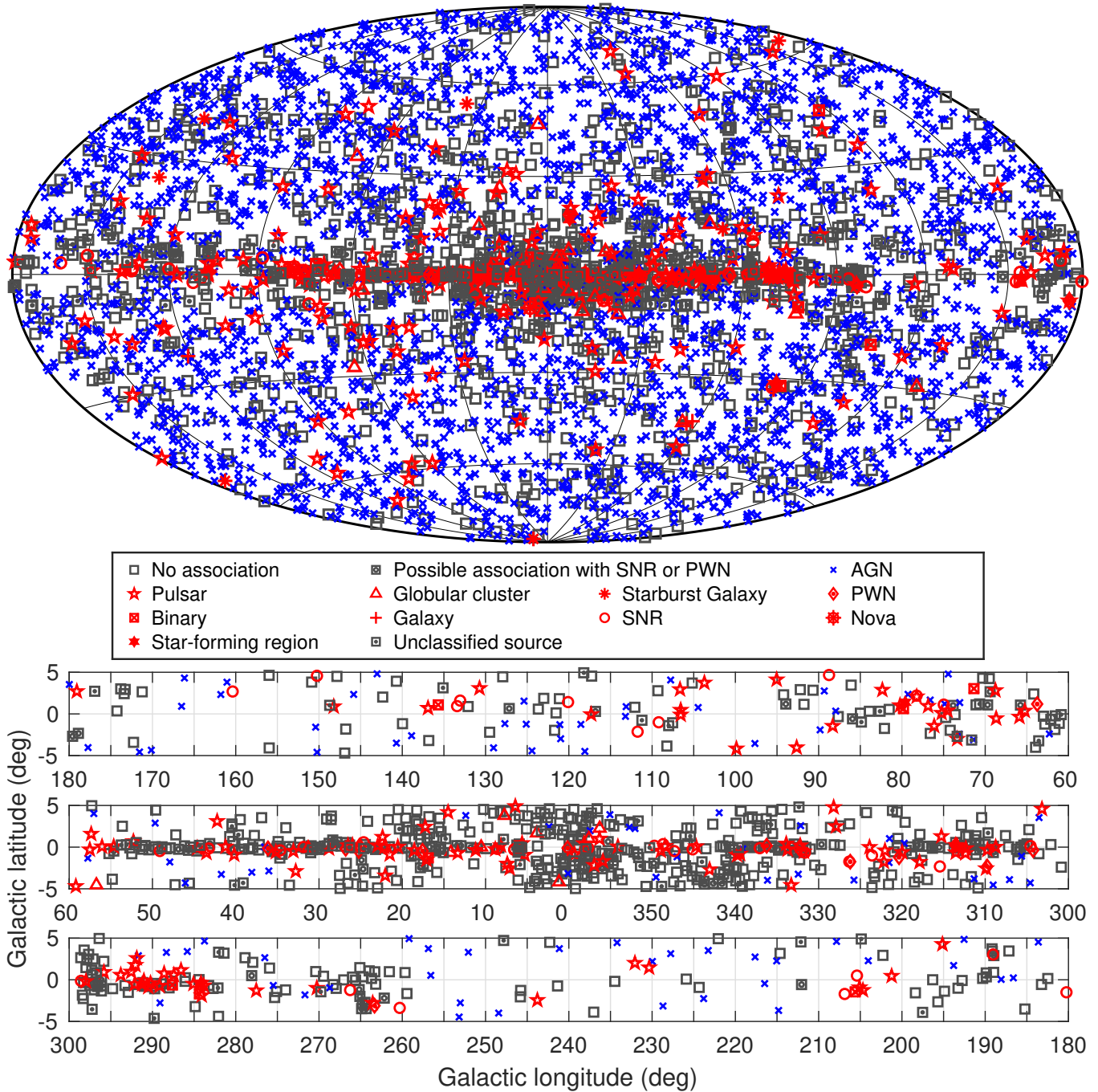


Figure 2. Full sky map (top) and blow-up of the Galactic plane split into three longitude bands (bottom) showing sources by source class (see Table 7, no distinction is made between associations and identifications). All AGN classes are plotted with the same blue symbol for simplicity. Other associations to a well-defined class are plotted in red. Unassociated sources and sources associated to counterparts of unknown nature are plotted in black.

553 likelihood bias in the 1FGL analysis, and also to the less accurate procedure then used to extract
 554 source flux (see discussion in the 2FGL paper).

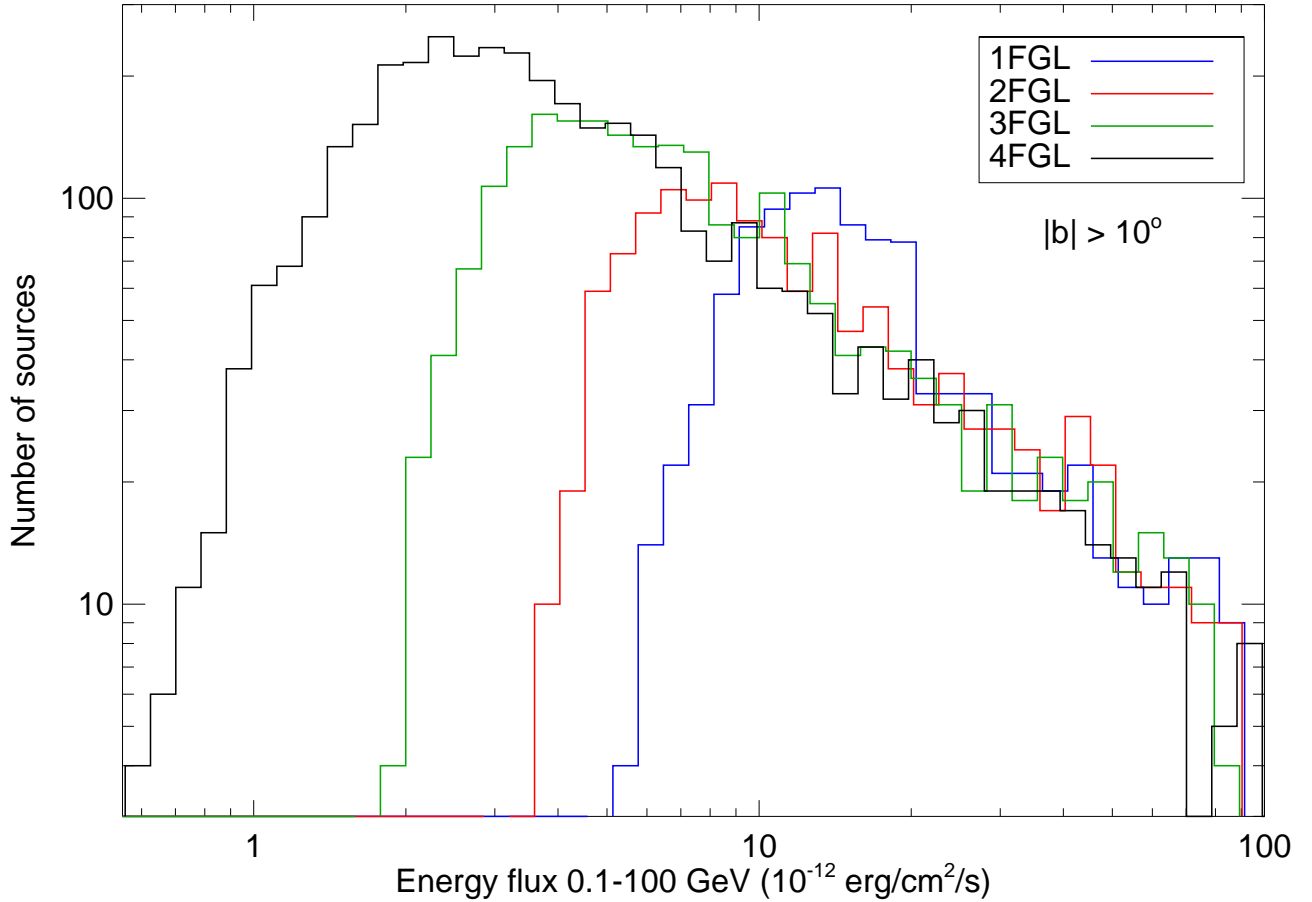


Figure 3. Distributions of the energy flux for the high-latitude sources ($|b| > 10^\circ$) in the 1FGL (1043 sources, blue), 2FGL (1319 sources, red), 3FGL (2193 sources, green) and 4FGL (3663 sources, black) catalogs, illustrating the approximate detection threshold.

555 The threshold at low flux is less sharp in 4FGL than it was in 2FGL or 3FGL. This reflects a
 556 larger dependence of the detection threshold on the power-law index. The detection threshold for
 557 soft sources decreases only slowly with exposure due to the weights (Appendix A).

558 The power-law index Γ is a way to compare all sources over all catalog generations, ignoring
 559 the complexities of the curved models. Figure 4 shows the four distributions of the power-law
 560 indices of the sources at high Galactic latitude are very similar. Their averages and widths are
 561 $\Gamma_{1\text{FGL}} = 2.22 \pm 0.33$, $\Gamma_{2\text{FGL}} = 2.17 \pm 0.30$, $\Gamma_{3\text{FGL}} = 2.22 \pm 0.31$ and $\Gamma_{4\text{FGL}} = 2.23 \pm 0.30$.

562 Small differences in the power-law index distributions could be related to slightly different
 563 systematic uncertainties in the effective area between the IRFs used respectively for 4FGL, 3FGL,
 564 2FGL, and 1FGL (Table 1). There is actually no reason why the distribution should remain the
 565 same, since the detection threshold depends on the index and the log N-log S of flat-spectrum radio
 566 quasars, which are soft *Fermi* sources, differs from that of BL Lacs, which are hard in the *Fermi* band
 567 (Ackermann et al. 2015, Fig. 7). The apparent constancy may largely be the result of competing
 568 effects.

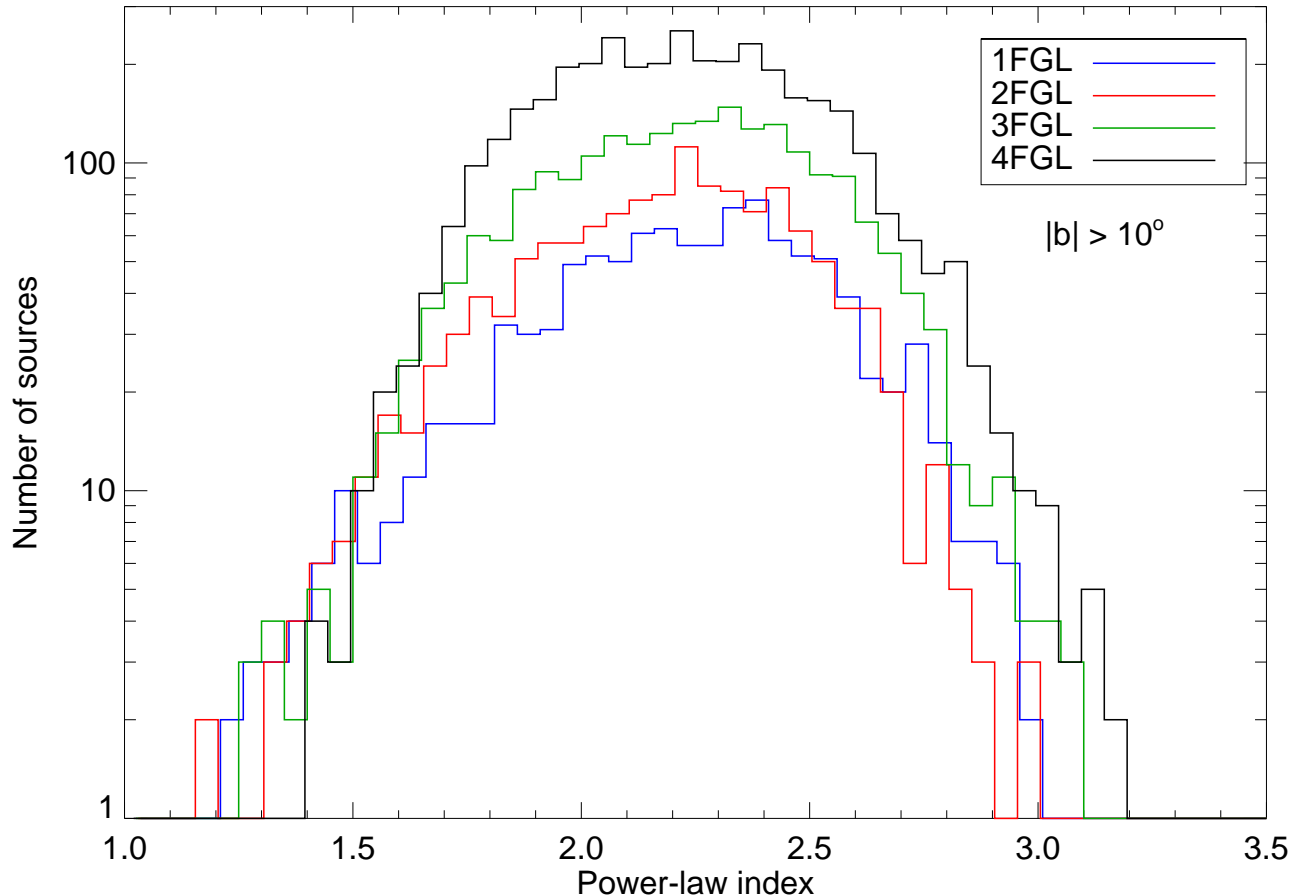


Figure 4. Distributions of the power-law index for the high-latitude sources in the 1FGL (blue), 2FGL (red), 3FGL (green) and 4FGL (black) catalogs. The sources are the same as in Fig 3.

569 We have compared the distribution of error radii (defined as the geometric mean of the semi-
 570 major and semi-minor axes of the 95% confidence error ellipse) of the 1FGL, 2FGL, 3FGL and
 571 4FGL sources at high Galactic latitude. Overall the source localization improves mechanically as
 572 more photons are added to previously detected sources. We concentrate instead on what happens
 573 specifically for faint sources. Figure 5 shows the distribution of 95% confidence error radii for those
 574 sources with $25 < TS < 100$ in any of the catalogs. The improvement at a given TS level is partly
 575 due to the event-level analysis (from Pass 6 to 7 and 8, see Table 1) and partly to the fact that, at a
 576 given significance level and for a given spectrum, fainter sources over longer exposures are detected
 577 with more photons. This improvement is key to preserving a high rate of source associations (§ 6)
 578 even though the source density increases.

579 *4.2.2. Step-by-step from 3FGL to 4FGL*

580 In order to understand the improvements of the 4FGL analysis with respect to 3FGL, we have
 581 considered the effects of changing the analysis and the data set without changing the time range (i.e.,
 582 leaving it as four years). To that end we started with the same seeds as the 3FGL catalog, changed

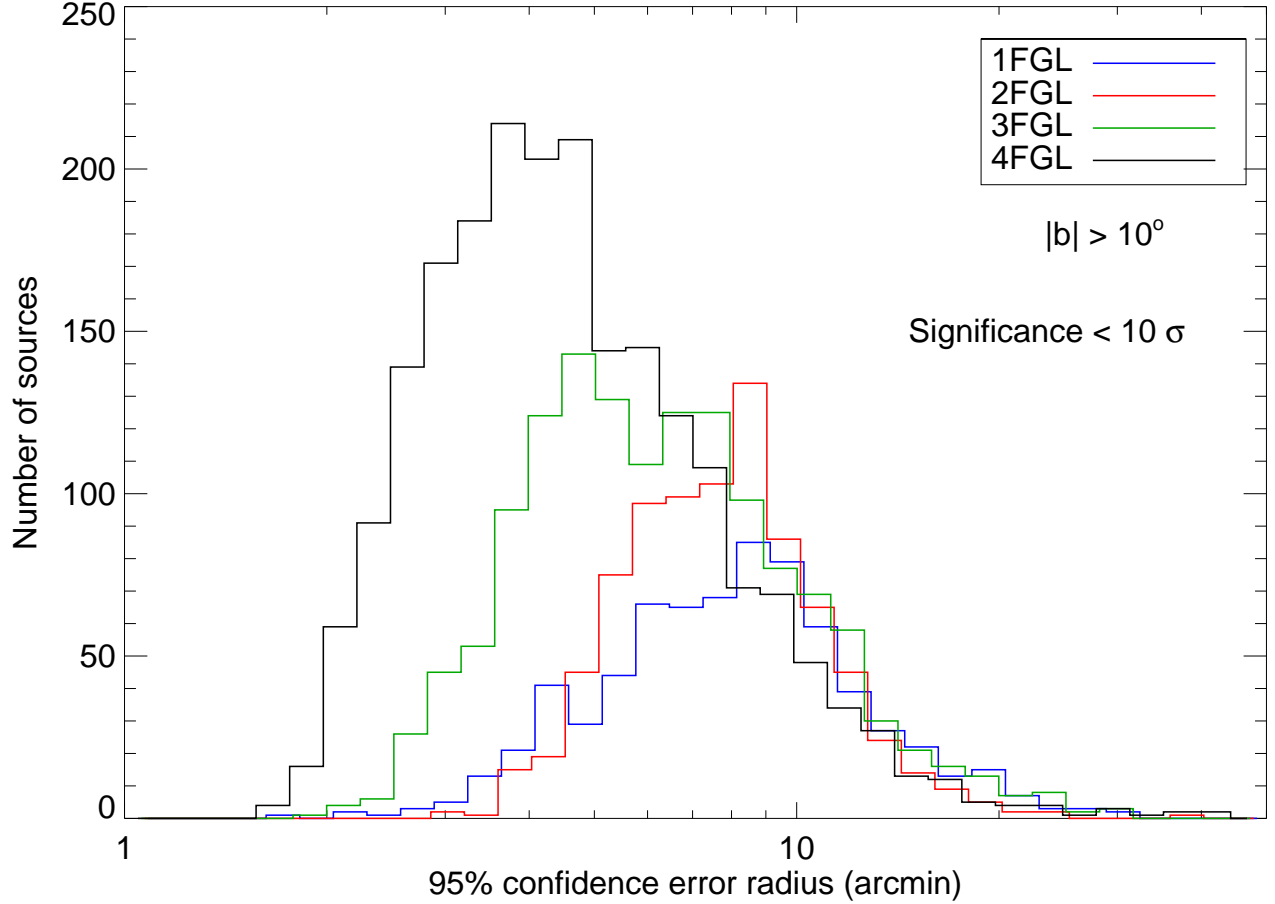


Figure 5. Distributions of the 95% confidence error radii for high-latitude sources with significance < 10 in 1FGL (713 sources, blue), 2FGL (843 sources, red), 3FGL (1387 sources, green) and 4FGL (2107 sources, black), illustrating the improvement of localizations for sources of equivalent detection significances.

583 each element in sequence (in the order of the list below) and compared each intermediate result with
 584 the previous one. The effect of introducing energy dispersion was described in § 3.2.

- 585
- 586 • We first switched from P7REP to Pass 8, eliminating the Earth limb by cutting zenith angles
 587 $< 90^\circ$ at 100 to 300 MeV and $< 97.5^\circ$ at 300 MeV to 1 GeV for Front, $< 80^\circ$ at 100 to 300 MeV
 588 and $< 95^\circ$ at 300 MeV to 1 GeV for Back. The resulting TS increased by 27%, in keeping with
 589 the effective area increase (the number of sources at $TS > 25$ did not rise, for lack of seeds).
 590 Energy flux decreased by 7% in faint sources. In the Galactic plane sources softened by 0.04
 591 on average. Both effects appear to be due to the diffuse emission modeling, because they are
 592 absent in the bright sources. The isotropic spectrum was recomputed, and even though the
 593 Galactic diffuse model was the same, its effects differed because the effective area increase with
 594 Pass8 is stronger at low energy. Those offsets are accompanied by a large scatter: only 72% of
 P7REP events are still in P8R3, and even for those the reconstructed direction differs.
 - 595 • Switching from Front/Back to PSF event types increased TS by 10% (140 more sources).
 596 This was the intended effect (keep good events and bad ones apart as much as possible). No

systematic effect was noted on energy flux. Soft sources got somewhat softer with PSF event types (power-law indices larger than 2.7 increased by 0.1 on average), but the bias averaged over all sources was only +0.01. The number of curved sources decreased by 50 and the curvature β by 0.025 (this is the same effect: low energies moved up, so spectra got closer to a power law).

- Applying the weights results in a general decrease of TS and increase of errors, as expected. However, because source detection is dominated by energies above 1 GeV even without weights, the effect is modest (the number of sources decreased by only 40). The difference is of course largest for soft sources and in the Galactic plane, where the background is larger and the weights are smaller. There are a few other side effects. The number of curved sources went down by 30. This is because the lever arm is less as low energies have been played down. The pivot energy tended to go up for the same reason, and this resulted in a softening of the power-law index of curved sources (not exceeding 0.1). Overall in the Galactic ridge the power-law index increased by 0.025.

We evaluated the other two changes on eight years of data:

- Changing the energy range to start at 50 MeV did not improve TS , as expected (the PSF is too broad below 100 MeV to contribute to significance). The energy flux (defined in the same 100 MeV to 100 GeV band) tended to go down in the Galactic plane (by as much as -10% in the Galactic ridge) and the power-law index tended to become harder (by as much as -0.05 in the Galactic ridge). This is because the low-energy information tends to stabilize artificially soft sources. Neither effect was noticeable outside the Galactic plane. The other consequence was to increase the number of significantly curved sources by 80, because the broader energy range made it easier to detect curvature (this was true everywhere in the sky).
- Changing the Galactic diffuse emission model from `gll_iem_v06` used in 3FGL to that used here (§ 2.4), without changing the analysis or the data. The flags in § 3.5.3 are based on comparing to a version of the FL8Y source list (using `gll_iem_v06`) extending the energy range to start at 50 MeV, but still differing from 4FGL in the extended sources and the energy bins in the first (50 – 100 MeV) component. Because of those differences the current flags are a little conservative. A detailed discussion of that effect is deferred to the full 4FGL release.

In conclusion, to first order the resulting net changes are not very large, consistent with the general comparison between 4FGL and 3FGL in § 4.2.1. Systematic effects are collectively visible but within calibration errors, and within statistical errors of individual sources.

5. AUTOMATED SOURCE ASSOCIATIONS

Table 6. Catalogs Used for the Automatic Source Association Methods

Name	Objects ^a	Ref.
High \dot{E}/d^2 pulsars	313	Manchester et al. (2005) ^b
Other normal pulsars	2248	Manchester et al. (2005) ^b

Table 6 continued on next page

Table 6 (continued)

Name	Objects ^a	Ref.
Millisecond pulsars	240	Manchester et al. (2005) ^b
Pulsar wind nebulae	69	Collaboration internal
High-mass X-ray binaries	137	Chaty et al. (2018)
Low-mass X-ray binaries	187	Liu et al. (2007)
Point-like SNR	158	Green (2014) ^c
Extended SNR ^f	295	Green (2014) ^c
Globular clusters	160	Harris (1996)
Dwarf galaxies ^f	100	McConnachie (2012)
Nearby galaxies	276	Schmidt et al. (1993)
IRAS bright galaxies	82	Sanders et al. (2003)
BZCAT (Blazars)	3561	Massaro et al. (2009)
BL Lac	1371	Véron-Cetty & Véron (2010)
AGN	10066	Véron-Cetty & Véron (2010)
QSO	129,853	Véron-Cetty & Véron (2010)
Seyfert galaxies	27651	Véron-Cetty & Véron (2010)
Radio loud Seyfert galaxies	29	Collaboration internal
Radio-loud Seyfert galaxies	556	Rakshit et al. (2017)
FRICAT (Radiogalaxies)	233	Capetti, A. et al. (2017a)
FRIICAT (Radiogalaxies)	123	Capetti, A. et al. (2017b)
Giant Radio Source	349	Kuźmicz et al. (2018)
2WHSP	1691	Chang et al. (2017)
WISE blazar catalog	12319	D’Abrusco et al. (2014)
Radio Fundamental Catalog	14786	http://astrogeo.org/rfc
CGRaBS	1625	Healey et al. (2008)
CRATES	11499	Healey et al. (2007)
ATCA 20 GHz southern sky survey	5890	Murphy et al. (2010)
105-month Swift/BAT catalog	1632	Oh et al. (2018)
4 th IBIS catalog	939	Bird et al. (2016)
1st AGILE catalog ^e	54	Pittori et al. (2009)
3rd EGRET catalog ^e	271	Hartman et al. (1999)
EGR catalog ^e	189	Casandjian & Grenier (2008)
0FGL list ^e	205	Abdo et al. (2009c, 0FGL)
1FGL catalog ^e	1451	Abdo et al. (2010a, 1FGL)
2FGL catalog ^e	1873	Nolan et al. (2012, 2FGL)
3FGL catalog ^e	3033	Acero et al. (2015, 3FGL)
1FHL catalog ^e	514	Ackermann et al. (2013, 1FHL)
2FHL catalog ^e	360	Ackermann et al. (2016b, 1FHL)
3FHL catalog ^e	1556	Ajello et al. (2017, 1FHL)
TeV point-like source catalog ^e	108	http://tevcat.uchicago.edu/
TeV extended source catalog ^f	72	http://tevcat.uchicago.edu/
LAT pulsars	234	Collaboration internal ^d
LAT identified	145	Collaboration internal

Table 6 continued on next page

Table 6 (*continued*)

Name	Objects ^a	Ref.
------	----------------------	------

^aNumber of objects in the catalog.

^bversion 1.56, <http://www.atnf.csiro.au/research/pulsar/psrcat>

^cGreen D. A., 2017, ‘A Catalogue of Galactic Supernova Remnants (2017 June version)’, Cavendish Laboratory, Cambridge, United Kingdom (available at <http://www.mrao.cam.ac.uk/surveys/snrs/>)

^d<https://confluence.slac.stanford.edu/display/GLAMCOG/Public+List+of+LAT-Detected+Gamma-Ray+Pulsars>

^eFor these catalogs, the association is performed by requiring that the separation from the 4FGL sources is less than the quadratic sum of the 99.9% confidence error radii.

^fFor these catalogs of extended sources, the association is performed by requiring that the separation from the 4FGL sources is less than the quadratic sum of the 95% confidence error radii.

629 The Bayesian method (Abdo et al. 2010a) for the *Fermi*-LAT, implemented with the *gtsrcid* tool⁸,
630 was developed following the prescription devised by Mattox et al. (1997) for EGRET. It relies on
631 the fact that the angular distance between a LAT source and a candidate counterpart is driven by
632 i) the position uncertainty in the case of a real association ii) the counterpart density in the case
633 of a false (random) association. In addition to the angular-distance probability density functions
634 for real and false associations, the posterior probability depends on a prior. This prior is calibrated
635 via Monte Carlo simulations so that the number of false associations, N_{false} is equal to the sum of
636 the association-probability complements. For a given counterpart catalog, the so-obtained prior is
637 found to be close to N_{assoc}/N_{tot} , where N_{assoc} is the number of associations from this catalog and
638 N_{tot} is the number of catalog sources. The sum of the association probabilities over all pairs (γ -ray
639 source, potential counterpart) gives the total number of real associations for a particular catalog. The
640 total numbers of associations are reported below for the various classes, where the overlap between
641 associations from different catalogs is taken into account. A uniform threshold of 0.8 is applied to the
642 posterior probability for the association to be retained. The reliability of the Bayesian associations is
643 assessed by verifying that the distribution of the angular offset between γ -ray source and counterpart
644 matches well the expected one in the case of a true association, i.e., a Rayleigh function with its
645 width parameter given by the sources positional uncertainties.

646 The list of counterpart catalogs, listed in Table 6, includes known γ -ray-emitting source classes:
647 Active Galactic Nuclei (AGN, Ackermann et al. (2015)), galaxies (Abdo et al. 2010g), pulsars (Abdo
648 et al. 2013), pulsar-wind nebulae (Ackermann et al. 2011c), supernova remnants (Acero et al. 2016c),
649 globular clusters (Abdo et al. 2010h), low- and high-mass X-ray binaries (Abdo et al. 2010i, 2009d) or
650 surveys of candidate blazars at other frequencies (radio, IR, X-rays). The reported source classes are
651 derived in the same way as in 3FGL. For non-AGN sources, this classification is based on the nature
652 of the association catalogs. For AGN, the subclasses as flat-spectrum radio quasars (FSRQ), BL Lac-
653 type objects (BLL), blazar candidates of uncertain type (BCU), radio galaxies (RDG), narrow-line
654 Seyfert 1 (NLSY1), steep spectrum radio quasar (SSRQ), Seyfert galaxies (SEY) or simply AGN (if no
655 other particular subclass can be assigned), have been selected according to the counterpart properties
656 at other wavelengths. Please note that we did not use the blazar classes from the Simbad database

⁸ <https://fermi.gsfc.nasa.gov/ssc/data/analysis/scitools/overview.html>

657 ⁹ since some of them correspond to predictions based on the WISE-strip approach (D’Abrusco et al.
658 2014) and not to assessment with the measured strengths of the emission lines.

659 In complement to the Bayesian method, the Likelihood-Ratio (LR) method (Ackermann et al.
660 2011b, 2015), following de Ruiter et al. (1977) provides supplementary associations with blazar
661 candidates based on large radio and X-ray surveys: NVSS (Condon et al. 1998), SUMSS (Mauch
662 et al. 2003), ROSAT (Voges et al. 1999, 2000) and AT20G (Murphy et al. 2010). This method is
663 similar in essence to the Bayesian method but the false association rate is derived from the density
664 of objects brighter than the considered candidate, assessed from the survey log N-log S distribution.
665 While the LR method is able to handle large surveys, its fraction of false associations is notably
666 larger than in the Bayesian method (typically 10% vs 2%). The overlap between the results of the
667 Bayesian and LR methods is about 75% for blazars. Because the surveys include a large number
668 of Galactic sources at low Galactic latitudes, the class of $|b| < 10^\circ$ sources associated solely via the
669 LR-method has been set to ‘UNK’ (standing for unknown) as opposed to the ‘BCU’ class used by
670 default for sources at larger latitudes.

671 The cross-correlation with previous γ -ray catalogs has been performed by requiring that the 99.9%
672 ellipse regions overlap (using $r_{99.9}/r_{95}=1.52$). Firm identifications are based on periodic variability
673 for LAT-detected pulsars or X-ray binaries, correlated variability at other wavelengths for AGN or
674 spatial morphology related to that found in another band for extended sources.

675

6. ASSOCIATION SUMMARY

676 The association summary is given in table 7. Out of 5099 LAT sources in 4FGL, 1525 are
677 unassociated (30%) or classified as “SPP” or as “unknown” (4% in total). Some 3257 sources are
678 associated with the Bayesian method (909 associations from this method only, overall $N_{false}=35.6$),
679 2612 sources with the LR method (264 associations from this method only, $N_{false}= 27.9$ for the
680 latter). The overall association fraction, 70%, is similar to that obtained in previous LAT catalogs.
681 It must be noted that the association fraction is lower for fainter sources (all bright sources are
682 associated), in particular due to their larger error regions. This fraction also drops as sources lie
683 closer to the Galactic plane as illustrated in Figure 6. It decreases from about 85% at high Galactic
684 latitudes to $\simeq 40\%$ close to the Galactic plane. The reason for such an effect is twofold. First,
685 the number of unassociated Galactic sources is large. Secondly, the flux limits of the extragalactic-
686 counterpart catalogs are larger due to extinction effects in these directions. The properties of the
687 unassociated sources are discussed below.

688 Sources reported as new below mean that they were not in previous FGL catalogs, although their
689 detections may have been reported in other works, e.g., Arsioli & Polenta (2018); Zhang et al. (2016),
690 or in specialized LAT catalogs.

691

6.1. Extragalactic sources

692

6.1.1. Active Galactic Nuclei

693 The largest source population in 4FGL is that of AGN, with 2938 blazars, 38 radio galaxies and
694 33 other AGN. The blazar sample comprises 681 flat-spectrum radio quasars (FSRQ), 1102 BL Lac-
695 type objects (BL Lac) and 1152 blazar candidates of unknown type (BCU) The detailed properties
696 of the 4FGL AGN, including redshifts and fitted synchrotron-peak positions, will be the subject of

⁹ <http://simbad.u-strasbg.fr/simbad/>

Table 7. LAT 4FGL Source Classes

Description	Identified		Associated	
	Designator	Number	Designator	Number
Pulsar, identified by pulsations	PSR	231
Pulsar, no pulsations seen in LAT yet	psr	10
Pulsar wind nebula	PWN	12	pwn	6
Supernova remnant	SNR	24	snr	16
Supernova remnant / Pulsar wind nebula	SPP	0	spp	92
Globular cluster	GLC	0	glc	30
Star-forming region	SFR	3	sfr	0
High-mass binary	HMB	5	hmb	3
Low-mass binary	LMB	1	lmb	1
Binary	BIN	1	bin	0
Nova	NOV	1	nov	0
BL Lac type of blazar	BLL	22	bll	1080
FSRQ type of blazar	FSRQ	42	fsrq	639
Radio galaxy	RDG	6	rdg	32
Non-blazar active galaxy	AGN	1	agn	16
Steep spectrum radio quasar	SSRQ	0	ssrq	2
Compact Steep Spectrum radio source	CSS	0	css	5
Blazar candidate of uncertain type	BCU	3	bcu	1152
Narrow line Seyfert 1	NLSY1	3	nlsy1	5
Seyfert galaxy	SEY	0	sey	1
Starburst galaxy	SBG	0	sbg	7
Normal galaxy (or part)	GAL	2	gal	2
Unknown	UNK	0	unk	118
Total	...	357	...	3217
Unassociated	1525

NOTE—The designation ‘spp’ indicates potential association with SNR or PWN. Designations shown in capital letters are firm identifications; lower case letters indicate associations.

697 the 4LAC companion catalog. We note here that the relative separation in γ -ray spectral hardness
 698 between FSRQs and BL Lacs already reported in previous LAC AGN catalogs is confirmed: 93% of
 699 FSRQs and 81% of BL Lacs have power-law photon indices greater and lower than 2.2 respectively.
 700 Among the 71 non-blazar AGN, 36 were present in the 3FGL. The 16 new radio galaxies are: 3C
 701 120, NGC 315, CRATES J070908.00+483655. NGC 3894, TXS 1303+114, B2.2 1447+27, PKS
 702 1514+00, TXS 1516+064, PKS B1518+045, PKS 1839–48, PKS 2153–69, PKS 2225–308, PKS
 703 2300–18, PKS 2324–02, PKS 2327–215, PKS 2338–295. Four 3FGL sources have changed classes
 704 to radio galaxies, all former bcu (TXS 0149+710, IC 4516, PKS 1304–215, CGCG 050–083) and one
 705 is missing: Cen B. The 33 ‘other AGN’ sources include five compact steep spectrum radio sources
 706 (CSS, three are new: 3C 138, 3C 216, 3C 309.1), two steep spectrum radio quasars (SSRQ, new is 3C
 707 212), 8 Narrow-line Seyferts 1 (NLSY1), one Seyfert galaxy (Circinus, SEY) and 17 AGN of other
 708 types (AGN). Three NLSY1 are new: IERS B1303+515, B3 1441+476, TXS 2116–077.

709

6.1.2. Other galaxies

710 No other nearby galaxies, besides the SMC, LMC, and M 31, are detected. Seven starburst galaxies
 711 in the IRAS catalog (Sanders et al. 2003) are associated with 4FGL sources. Two sources, Arp 220

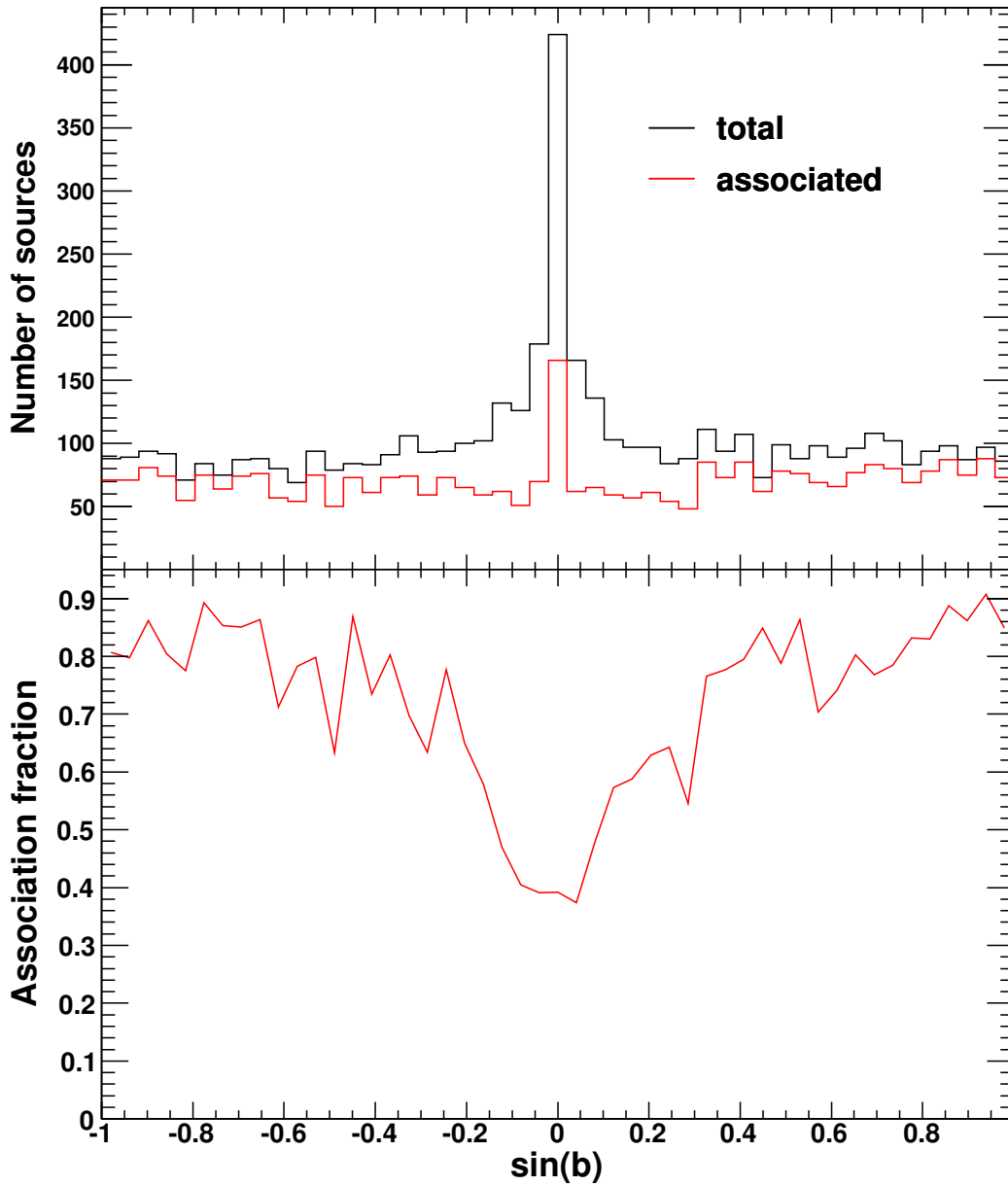


Figure 6. Upper panel: Distributions in Galactic latitude b of 4FGL sources (black histogram) and associated sources (blue histogram). Lower panel: Association fraction as a function of Galactic latitude.

712 (Peng et al. 2016; Griffin et al. 2016; Yoast-Hull et al. 2017) and NGC 2146 (Tang et al. 2014), have
 713 been reported as LAT detections since the 3FGL release. Yoast-Hull et al. (2017) found an excess
 714 of γ rays over the expected starburst contribution in Arp 220, similar to the case of the Circinus
 715 galaxy (Hayashida et al. 2013). NGC 2146 being close (0.1°) to the FSRQ 1REX J061757+7816.1,
 716 the association is ambiguous. We favor the NGC 2146 association as no evidence for variability is
 717 found and the 4FGL photon index (2.16) is somewhat low for a FSRQ. Another source, NGC 3424,
 718 was not present in 3FGL. The IRAS source UGC 11041, which could have been classified as sbg
 719 shows significant variability in the LAT band, so the γ -ray emission most likely arises from an AGN

(there is a flat-spectrum radio source, MG2 J175448+3442 at a distance of 2.4') and it is classified as such. In addition to these seven associations, the Bayesian method predicts that three more 4FGL sources should be starburst galaxies. Some 4FGL sources are positionally consistent with known galaxy clusters, but these clusters host radio galaxies which are the most likely emitters. No dwarf galaxies have been detected.

6.2. Galactic sources

The Galactic sources include:

- 241 pulsars (PSR). The public list of LAT-detected pulsars is regularly updated¹⁰. Some 231 pulsars in this list are included in 4FGL (67 would have been missed by the association pipeline using the ATNF catalog), while 4 are absent because they did not pass the TS>25 criterion. These pulsars represent by far the largest population of identified sources in 4FGL. Another 10 pulsars from the ATNF database are associated with 4FGL sources with high-confidence via the Bayesian method. This method predicts that about 30 extra 4FGL sources are ATNF pulsars. Note that out of the 24 pulsar candidates presented in 3FGL, pulsations have now been detected for 18 of them. The other 6 are not associated with pulsars in 4FGL anymore.
- 40 supernova remnants (SNR). Out of them, 24 are extended and thus firmly identified. The other 16 are not resolved. SNR G150.3+4.5 having a logp-normal spectral shape with a very hard photon index, Γ of 1.6 indicates that the emission is most likely leptonic and makes this source an excellent candidate for the Cherenkov Telescope Array (CTA). In contrary, the softer spectrum of SNR N132D (photon index=2.07) makes the hypothesis of a dominant hadronic emission likely. The significant spectral curvature seen in Puppis A is in accord with its non-detection in the TeV domain.
- 18 pulsar wind nebulae (PWN), 15 of them being extended. New additions are N 157B, PWN G63.7+1.1, HESS J1356–645, FGES J1631.6–4756, FGES J1836.5–0651, FGES J1838.9–0704, HESS J1857+026. The median photon index of the 4FGL PWN is 2.31. N 157B, located in LMC, has a photon index of 2.0, hinting at an additional contribution from a (yet-undetected pulsar at low energy on top of the PWN).
- 92 sources (referred to as SPP) of unknown nature but overlapping with known SNR or PWN and thus candidates to these classes. The estimation of missed associations of SNR, PWNe and SPP sources is made difficult by the intrinsic spatial extension of the sources; no attempts have thus been made along this line.
- 30 globular clusters (GLC). Missing relative to 3FGL is 2MS-GC01. The 16 new associations are NGC 362, NGC 1904, NGC 5286, NGC 5904, NGC 6139, NGC 6218, NGC 6304, NGC 6341, Terzan 2, Terzan 1, NGC 6402, NGC 6397, GLIMPSE02, GLIMPSE01, NGC 6838, NGC 7078. Only 2 extra 4FGL sources are estimated to be globular clusters.
- Six high-mass X-ray binaries (HMB). The three new sources are HESS J0632+057, which has a reported LAT detection after the 3FGL (Li et al. 2017b), RX J0648.0– 4418/HD 49798,

¹⁰ See <https://confluence.slac.stanford.edu/display/GLAMCOG/Public+List+of+LAT-Detected+Gamma-Ray+Pulsars>

757 which is a peculiar X-ray binary (Mereghetti et al. 2011; Popov et al. 2018), and Cyg X-1,
 758 an archetypical black-hole binary reported after the 3FGL (Zdziarski et al. 2017; Zanin et al.
 759 2016). Three extra 4FGL sources are estimated to be HMB according to the Bayesian method.

- 760 • Three star-forming regions; new since 3FHL is the association of the extended source FHES
 761 J1626.9–2431 (§ 3.4) with the ρ Ophiuchi star-forming region.
- 762 • Two low-mass X-ray binaries (LMB). PSR J1023+0038 is a known binary MSP/LXB transition
 763 system, with a change in γ -ray flux detected (Stappers et al. 2014) simultaneously with a state
 764 change, and was previously detected as 2FGL J1023.6+0040 (but not detected in the 3FGL).
 765 The LMB 2S 0921–630 (V395 Car) is a well-studied binary involving a neutron star and a K0
 766 III star with an orbital period of 9 days (Shahbaz & Watson 2007) and is a new LAT detection.
- 767 • One binary star (BIN), η Carinae.
- 768 • One nova, V5668 Sagittarii. Other novae detected by the LAT are missing. Novae have short
 769 durations, and most are below the significance threshold because their signal is diluted over
 770 the eight years of 4FGL data.

6.3. Unassociated sources

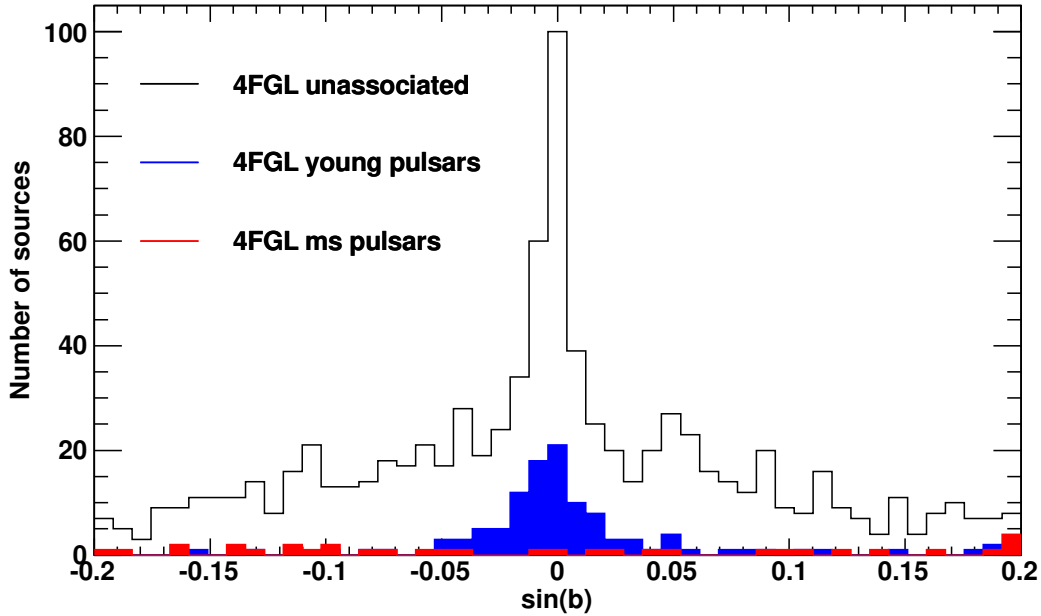


Figure 7. Distributions in Galactic latitude b of 4FGL unassociated sources (black histogram) compared to those of LAT-detected pulsars (young pulsars: blue histogram, millisecond pulsars: red histogram).

772 Out of the 1528 sources unassociated in 4FGL, 376 already present in 3FGL had no associations
 773 there. Another 32 sources previously associated in 3FGL have now lost their associations because of
 774 a shift in their locations relative to 3FGL.

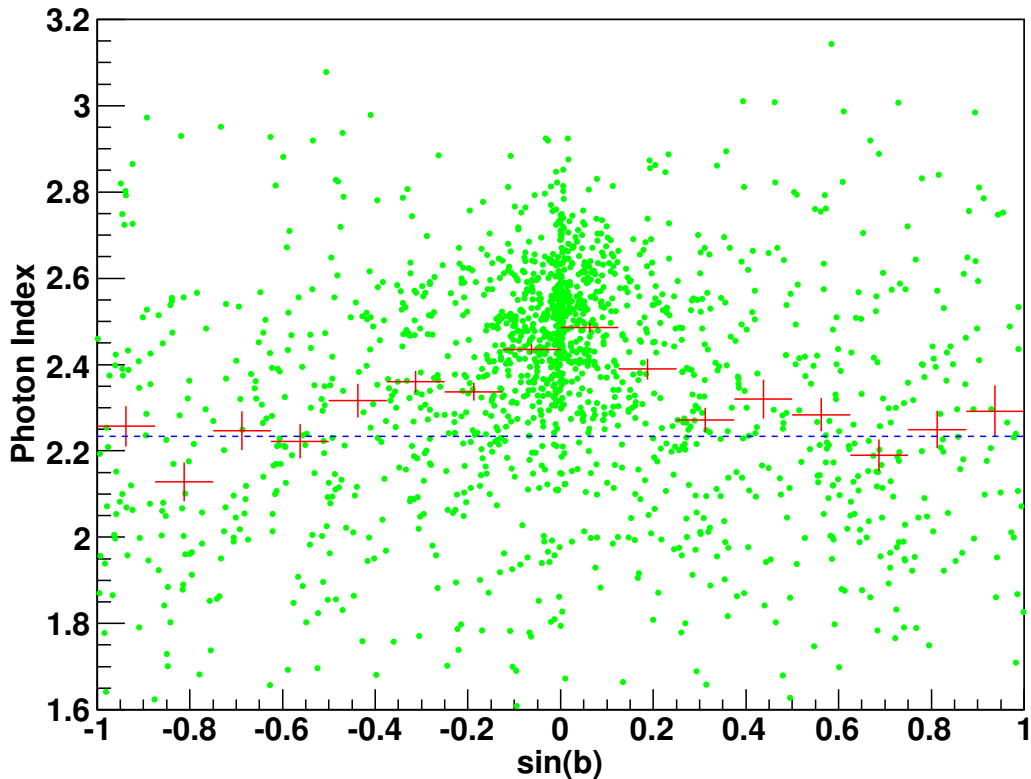


Figure 8. Green symbols: Power-law photon index versus Galactic latitude, b , for the unassociated 4FGL sources. Red bars: average photon index for different bins in b . Dashed blue line: average photon index of 4FGL BCU blazars.

775 About half of the unassociated sources are located less than 10° away from the Galactic plane. Their
 776 wide latitude extension is hard to reconcile with those of known classes of Galactic γ -ray sources. For
 777 instance, Figure 7 compares this latitude distribution with that of LAT pulsars. In addition to nearby
 778 millisecond pulsars, which have a quasi isotropic distribution, the LAT detects only young isolated
 779 pulsars (age $< 10^6$ y) which are by nature clustered close to the plane. Older pulsars, which have
 780 had time to drift further off the plane, show a wider Galactic-latitude distribution, more compatible
 781 with the observed distribution of the unassociated sources, but these pulsars have crossed the ‘ γ -
 782 ray death line’ and are hence undetectable. Attempts to spatially cross correlate the unassociated
 783 population with other potential classes, e.g., LXMB (Liu et al. 2007), O stars¹¹, B stars¹² have been
 784 unsuccessful. The observed clustering of these unassociated sources in high-density ‘hot spots’ may
 785 be a clue that they actually correspond to yet-to-be identified, relatively nearby extended sources.
 786 The Galactic latitude distribution near the plane is clearly non-gaussian as visible in Figure 7, which
 787 may indicate the presence of several components.

788 The spectral properties of these sources as well can provide insight into their nature, as illustrated
 789 in Figure 8 showing the power-law photon index versus the Galactic latitude. The change in spectral

¹¹ GOSC <https://gosc.cab.inta-csic.es/>

¹² BeSS <http://basebe.obspm.fr/basebe/>

790 hardness with sky location demonstrates the composite nature of the unassociated population. The
 791 high-latitude sources shows an average photon index compatible with that of blazars of unknown type
 792 ($\Gamma=2.24$), a hint that these sources could predominantly be blazars. Unassociated sources lying closer
 793 to the Galactic plane have softer spectra, closer to that expected of young pulsars ($\Gamma=2.42$). Another
 794 interesting possibility is that some of these unassociated sources actually correspond to WIMP dark
 795 matter annihilating in Galactic subhalos (Ackermann et al. 2012d; Coronado et al. 2019). Indeed,
 796 Λ CDM cosmology predicts the existence of thousands of them below $\sim 10^7 M_\odot$, i.e., not massive
 797 enough to retain gas or stars at all. As a result, they are not expected to emit at other wavelengths
 798 and therefore they would not possess astrophysical counterparts. Interestingly, this dark matter
 799 annihilation may yield a pulsar-like spectrum (?).

800 6.4. Sources missing from previous catalogs

801 Out of 3033 3FGL sources, 406 are missing in 4FGL for various reasons, including the change of
 802 diffuse emission model, point sources being absorbed into new extended ones or variability effects.
 803 Most of these missing sources had low significance in 3FGL. Only 74 sources were associated. The
 804 majority are blazars (32 BCU, 15 FSRQ, 1 BLL and 1 SSRQ) plus one AGN. It is remarkable that
 805 while BLL are 36% more numerous relative to FSRQ in 3FGL, a much lower fraction (by a factor of
 806 20) has gone away in 4FGL, an effect possibly related to the larger variability of FSRQ relative to BLL
 807 observed in the LAT energy band (Ackermann et al. 2015). Other missing sources include 19 SPP, 3
 808 PSR and one PWN. The nova V407 Cyg is now missing as it no longer fulfills the average-significance
 809 criterion.

810 Concerning sources missing from 3FHL, established with the same data set, they amount to 30,
 811 with 14 unassociated, 10 blazars (4 BLL and 6 BCU), 1 AGN, 4 ‘unknown’ and the HMB PSR
 812 B1259–63. All these sources had a TS close to the TS=25 significance threshold.

813 6.5. TeV sources

Table 8. Associations of 4FGL with Extended TeV Sources

TeVcat Name ^a	4FGL Name
Boomerang	J2229.0+6114
CTA 1	J0007.0+7303
CTB 37A	J1714.4–3830
CTB 37B	J1714.1–3811
Crab	J0534.5+2201e
G318.2+00.1	J1453.4–5858
Geminga	J0633.9+1746
HESS J1018–589 B	J1016.3–5857
HESS J1026–582	J1028.5–5819
HESS J1303–631	J1303.0–6312e
HESS J1356–645	J1355.2–6420e
HESS J1420–607	J1420.3–6046e
HESS J1427–608	J1427.8–6051
HESS J1458–608	J1456.7–6050, J1459.5–6053
HESS J1507–622	J1507.9–6228e

Table 8 continued on next page

Table 8 (*continued*)

TeVcat Name ^a	4FGL Name
HESS J1534–571	J1533.9–5712e
HESS J1614–518	J1615.3–5146e
HESS J1616–508	J1616.2–5054e
HESS J1632–478	J1633.0–4746e
HESS J1640–465	J1640.6–4632
HESS J1702–420	J1705.7–4124
HESS J1718–385	J1718.2–3825
HESS J1729–345	J1730.1–3422
HESS J1745–303	J1745.8–3028e
HESS J1800–240 A	J1801.8–2358
HESS J1800–240B	J1800.2–2403 , J1800.7–2355 , J1800.9–2407
HESS J1804–216	J1804.7–2144e
HESS J1808–204	J1808.2–2028e
HESS J1809–193	J1810.3–1925e
HESS J1813–126	J1813.4–1246
HESS J1813–178	J1813.1–1737e
HESS J1825–137	J1824.5–1351e
HESS J1826–130	J1826.1–1256
HESS J1834–087	J1834.5–0846e
HESS J1841–055	J1840.9–0532e
HESS J1848–018	J1847.2–0141, J1848.6–0202, J1848.7–0129
HESS J1857+026	J1857.7+0246e
HESS J1858+020	J1858.3+0209
HESS J1912+101	J1911.7+1014, J1912.7+0957, J1913.3+1019
IC 443	J0617.2+2234e
Kookaburra (Rabbit)	J1417.7–6057, J1418.7–6057
Kookaburra PWN	J1420.0–6048
MGRO J1908+06	J1906.2+0631, J1907.9+0602
MGRO J2031+41	J2028.6+4110e
MSH 15–52	J1514.2–5909e
RCW 86	J1443.0–6227e
RX J0852.0–4622	J0851.9–4620e
RX J1713.7–3946	J1713.5–3945e
SNR G292.2–00.5	J1119.1–6127
TeV J1626-490	J1628.2-4848
Terzan 5	J1748.0–2446
VER J2019+407	J2021.0+4031e
Vela X	J0833.1-4511e
W 28	J1801.3–2326e
W 51	J1923.2+1408e
Westerlund 1	J1645.8–4533, J1648.4–4611, J1649.2–4513, J1650.3–4600, J1652.2–4516
Westerlund 2	J1023.3–5747e

^aFrom <http://tevcat.uchicago.edu>.

814 The synergy between the LAT and the Cherenkov telescopes operating in the TeV energy domain
815 has proven extremely fruitful, in particular by bringing out promising TeV candidates in the LAT
816 catalogs. This approach, further motivated by the upcoming deployment of the Cherenkov Telescope
817 Array, has justified the release of LAT source catalogs above 10 GeV, like the 3FHL (Ajello et al. 2017)

818 based on 7 years of data. The associations of 4FGL sources with extended sources listed in TeVCat¹³
 819 are presented in Table 8. Relative to 3FHL, 9 new extended TeV sources are associated with 4FGL
 820 extended sources (TeV sources: HESS J1534–571, HESS J1808–204, HESS J1809–193, see § 3.4), or
 821 (sometimes multiple) 4FGL point sources (TeV sources: HESS J1718–385, HESS J1729–345, HESS
 822 J1848–018, HESS J1858+020, MGRO J1908+06, HESS J1912+101). All TeV blazars have 4FGL
 823 counterparts. The median value of Γ for 4FGL point sources associated with TeV point sources is
 824 1.95, indicating hard spectra as expected. In associations with extended TeV sources, the median Γ
 825 changes from 2.09 to 2.38 depending on whether the 4FGL sources are extended or not. This fairly
 826 large difference favors the interpretation that most associations between extended TeV sources and
 827 non-extended 4FGL sources are accidental.

828 6.6. Counterpart positions

829 Whenever a high-confidence association with a point-like counterpart is obtained, we provide the
 830 most accurate counterpart position available and its uncertainty. In particular, 2277 4FGL AGN
 831 have Very Long Baseline Interferometry (VLBI) counterparts. VLBI, i.e., radio interferometry with
 832 baseline lengths of >1000 km is sensitive to radio emission from compact regions of AGN that are
 833 smaller than 20 mas, which corresponds to parsec scales. Such observations allow the determination
 834 of positions of the AGN jet base with milliarcsecond level accuracy. We used the Radio Fundamental
 835 Catalog¹⁴ based on the dedicated on-going observing program (Schinzel et al. 2015, 2017) with the
 836 Very Long Baseline Array (Napier et al. 1994), as well as VLBI data under other programs. The
 837 association between γ -ray source and VLBI counterpart was carried out along a similar, but distinct,
 838 scheme as that presented in § 5. This scheme (see Petrov et al. (2013) for more details) is based on
 839 the strong connection between the γ -ray emission and radio emission at parsec scales and on the sky
 840 density of bright compact radio sources being relatively low. The chance to find a bright background,
 841 unrelated compact radio source within the LAT positional error ellipse is low enough to establish
 842 association. The likelihood ratio (with a somewhat different definition from that implemented in
 843 the LR-method) was required to be greater than 8 to claim an association, with an estimated false
 844 association fraction of 1%.

845 For AGN without VLBI counterparts, the position uncertainties were set to typical values of
 846 $20''$ for sources associated from the RASS survey and $10''$ otherwise. For identified pulsars, the
 847 position uncertainties come from the rotation ephemeris used to find γ -ray pulsations, many of which
 848 were obtained from radio observations (Smith et al. 2019). If the ephemeris does not include the
 849 uncertainties and for pulsar candidates, we use the ATNF psrcat values. If neither of those exist, we
 850 use the 0.1° uncertainties from the list maintained by the WVU Astrophysics group¹⁵. Ephemeris
 851 position uncertainties are often underestimated, so we arbitrarily apply a minimum uncertainty of
 852 1 mas. For globular clusters from Harris (1996), the position uncertainties were assigned a typical
 853 value of $2''$ ¹⁶.

854 The *Fermi* LAT Collaboration acknowledges generous ongoing support from a number of agencies
 855 and institutes that have supported both the development and the operation of the LAT as well as
 856 scientific data analysis. These include the National Aeronautics and Space Administration and the

¹³ <http://tevcat.uchicago.edu/>

¹⁴ Available at <http://astrogeo.org/rfc>

¹⁵ <http://astro.phys.wvu.edu/GalacticMSPs/GalacticMSPs.txt>

¹⁶ <https://heasarc.gsfc.nasa.gov/w3browse/all/globclust.html>

857 Department of Energy in the United States, the Commissariat à l’Energie Atomique and the Centre
 858 National de la Recherche Scientifique / Institut National de Physique Nucléaire et de Physique des
 859 Particules in France, the Agenzia Spaziale Italiana and the Istituto Nazionale di Fisica Nucleare in
 860 Italy, the Ministry of Education, Culture, Sports, Science and Technology (MEXT), High Energy
 861 Accelerator Research Organization (KEK) and Japan Aerospace Exploration Agency (JAXA) in
 862 Japan, and the K. A. Wallenberg Foundation, the Swedish Research Council and the Swedish National
 863 Space Board in Sweden.

864 Additional support for science analysis during the operations phase is gratefully acknowledged from
 865 the Istituto Nazionale di Astrofisica in Italy and the Centre National d’Études Spatiales in France.
 866 This work performed in part under DOE Contract DE-AC02-76SF00515.

867 This work made extensive use of the ATNF pulsar catalog¹⁷ (Manchester et al. 2005). This
 868 research has made use of the NASA/IPAC Extragalactic Database (NED) which is operated by
 869 the Jet Propulsion Laboratory, California Institute of Technology, under contract with the National
 870 Aeronautics and Space Administration, and of archival data, software and online services provided
 871 by the ASI Science Data Center (ASDC) operated by the Italian Space Agency.

872 This research has made use of Aladin¹⁸, TOPCAT¹⁹ and APLpy, an open-source plotting package
 873 for Python²⁰. The authors acknowledge the use of HEALPix²¹ (Górski et al. 2005). The extended
 874 sources were taken from the Manitoba SNR catalog (Ferrand & Safi-Harb 2012).

875 *Facility:* Fermi LAT

REFERENCES

- 876 Abdo, A. A., Ackermann, M., Ajello, M., et al.
 877 2009a, *Astroparticle Physics*, 32, 193,
 878 doi: [10.1016/j.astropartphys.2009.08.002](https://doi.org/10.1016/j.astropartphys.2009.08.002)
 879 —. 2009b, *ApJL*, 706, L1,
 880 doi: [10.1088/0004-637X/706/1/L1](https://doi.org/10.1088/0004-637X/706/1/L1)
 881 —. 2009c, *ApJS*, 183, 46,
 882 doi: [10.1088/0067-0049/183/1/46](https://doi.org/10.1088/0067-0049/183/1/46)
 883 —. 2009d, *ApJL*, 701, L123,
 884 doi: [10.1088/0004-637X/701/2/L123](https://doi.org/10.1088/0004-637X/701/2/L123)
 885 —. 2010a, *ApJS*, 188, 405,
 886 doi: [10.1088/0067-0049/188/2/405](https://doi.org/10.1088/0067-0049/188/2/405)
 887 —. 2010b, *ApJ*, 712, 459,
 888 doi: [10.1088/0004-637X/712/1/459](https://doi.org/10.1088/0004-637X/712/1/459)
 889 —. 2010c, *ApJ*, 713, 146,
 890 doi: [10.1088/0004-637X/713/1/146](https://doi.org/10.1088/0004-637X/713/1/146)
 891 —. 2010d, *Science*, 328, 725,
 892 doi: [10.1126/science.1184656](https://doi.org/10.1126/science.1184656)
 893 —. 2010e, *ApJ*, 718, 348,
 894 doi: [10.1088/0004-637X/718/1/348](https://doi.org/10.1088/0004-637X/718/1/348)
 895 —. 2010f, *Science*, 327, 1103,
 896 doi: [10.1126/science.1182787](https://doi.org/10.1126/science.1182787)
 897 —. 2011, *ApJ*, 734, 116,
 898 doi: [10.1088/0004-637X/734/2/116](https://doi.org/10.1088/0004-637X/734/2/116)
 899 Abdo, A. A., Ajello, M., Allafort, A., et al. 2013,
 900 *ApJS*, 208, 17,
 901 doi: [10.1088/0067-0049/208/2/17](https://doi.org/10.1088/0067-0049/208/2/17)
 902 Abdo, A. A., et al. 2010g, *ApJL*, 709, L152,
 903 doi: [10.1088/2041-8205/709/2/L152](https://doi.org/10.1088/2041-8205/709/2/L152)
 904 —. 2010h, *A&A*, 524, A75+,
 905 doi: [10.1051/0004-6361/201014458](https://doi.org/10.1051/0004-6361/201014458)
 906 —. 2010i, *ApJ*, 723, 649,
 907 doi: [10.1088/0004-637X/723/1/649](https://doi.org/10.1088/0004-637X/723/1/649)
 908 Abramowski, A., Aharonian, F., Ait Benkhali, F.,
 909 et al. 2015, *A&A*, 574, A27,
 910 doi: [10.1051/0004-6361/201322694](https://doi.org/10.1051/0004-6361/201322694)
 911 Acero, F., Ackermann, M., Ajello, M., et al. 2015,
 912 *ApJS*, 218, 23,
 913 doi: [10.1088/0067-0049/218/2/23](https://doi.org/10.1088/0067-0049/218/2/23)
 914 —. 2016a, *ApJS*, 223, 26,
 915 doi: [10.3847/0067-0049/223/2/26](https://doi.org/10.3847/0067-0049/223/2/26)

¹⁷ <http://www.atnf.csiro.au/research/pulsar/psrcat>

¹⁸ <http://aladin.u-strasbg.fr/>

¹⁹ <http://www.star.bristol.ac.uk/~mbt/topcat/>

²⁰ <http://aplpy.github.com>

²¹ <http://healpix.jpl.nasa.gov/>

- 916 —. 2016b, *ApJS*, 224, 8,
917 doi: [10.3847/0067-0049/224/1/8](https://doi.org/10.3847/0067-0049/224/1/8)
- 918 —. 2016c, *ApJS*, 224, 8,
919 doi: [10.3847/0067-0049/224/1/8](https://doi.org/10.3847/0067-0049/224/1/8)
- 920 Ackermann, M., Ajello, M., Albert, A., et al.
921 2012a, *ApJS*, 203, 4,
922 doi: [10.1088/0067-0049/203/1/4](https://doi.org/10.1088/0067-0049/203/1/4)
- 923 —. 2016a, *PhRvD*, 93, 082001,
924 doi: [10.1103/PhysRevD.93.082001](https://doi.org/10.1103/PhysRevD.93.082001)
- 925 Ackermann, M., Ajello, M., Allafort, A., et al.
926 2011a, *Science*, 334, 1103
- 927 —. 2011b, *ApJ*, 743, 171,
928 doi: [10.1088/0004-637X/743/2/171](https://doi.org/10.1088/0004-637X/743/2/171)
- 929 —. 2012b, *Astroparticle Physics*, 35, 346,
930 doi: [10.1016/j.astropartphys.2011.10.007](https://doi.org/10.1016/j.astropartphys.2011.10.007)
- 931 —. 2013, *ApJS*, 209, 34,
932 doi: [10.1088/0067-0049/209/2/34](https://doi.org/10.1088/0067-0049/209/2/34)
- 933 Ackermann, M., Ajello, M., Atwood, W. B., et al.
934 2012c, *ApJ*, 750, 3,
935 doi: [10.1088/0004-637X/750/1/3](https://doi.org/10.1088/0004-637X/750/1/3)
- 936 —. 2015, *ApJ*, 810, 14,
937 doi: [10.1088/0004-637X/810/1/14](https://doi.org/10.1088/0004-637X/810/1/14)
- 938 —. 2016b, *ApJS*, 222, 5,
939 doi: [10.3847/0067-0049/222/1/5](https://doi.org/10.3847/0067-0049/222/1/5)
- 940 Ackermann, M., Ajello, M., Baldini, L., , et al.
941 2018, *ApJS*, 237, 32,
942 doi: [10.3847/1538-4365/aacdf7](https://doi.org/10.3847/1538-4365/aacdf7)
- 943 Ackermann, M., Ajello, M., Baldini, L., et al.
944 2016c, *ApJ*, 826, 1,
945 doi: [10.3847/0004-637X/826/1/1](https://doi.org/10.3847/0004-637X/826/1/1)
- 946 —. 2017, *ApJ*, 843, 139,
947 doi: [10.3847/1538-4357/aa775a](https://doi.org/10.3847/1538-4357/aa775a)
- 948 Ackermann, M., Albert, A., Atwood, W. B., et al.
949 2016d, *A&A*, 586, A71,
950 doi: [10.1051/0004-6361/201526920](https://doi.org/10.1051/0004-6361/201526920)
- 951 Ackermann, M., et al. 2011c, *ApJ*, 726, 35,
952 doi: [10.1088/0004-637X/726/1/35](https://doi.org/10.1088/0004-637X/726/1/35)
- 953 Ackermann, M., Ajello, M., Atwood, W. B., et al.
954 2012d, *ApJ*, 761, 91,
955 doi: [10.1088/0004-637X/761/2/91](https://doi.org/10.1088/0004-637X/761/2/91)
- 956 Aharonian, F., Akhperjanian, A. G., Aye, K.-M.,
957 et al. 2005, *A&A*, 439, 1013,
958 doi: [10.1051/0004-6361:20053195](https://doi.org/10.1051/0004-6361:20053195)
- 959 Aharonian, F., Akhperjanian, A. G., Barres de
960 Almeida, U., et al. 2008, *A&A*, 477, 353,
961 doi: [10.1051/0004-6361:20078516](https://doi.org/10.1051/0004-6361:20078516)
- 962 Ajello, M., Allafort, A., Baldini, L., et al. 2012,
963 *ApJ*, 744, 80, doi: [10.1088/0004-637X/744/1/80](https://doi.org/10.1088/0004-637X/744/1/80)
- 964 Ajello, M., Atwood, W. B., Baldini, L., et al. 2017,
965 *ApJS*, 232, 18, doi: [10.3847/1538-4365/aa8221](https://doi.org/10.3847/1538-4365/aa8221)
- 966 Ajello, M., Baldini, L., Barbiellini, G., et al. 2016,
967 *ApJ*, 819, 98, doi: [10.3847/0004-637X/819/2/98](https://doi.org/10.3847/0004-637X/819/2/98)
- 968 Araya, M. 2014, *MNRAS*, 444, 860,
969 doi: [10.1093/mnras/stu1484](https://doi.org/10.1093/mnras/stu1484)
- 970 Araya, M. 2017, *ApJ*, 843, 12,
971 doi: [10.3847/1538-4357/aa7261](https://doi.org/10.3847/1538-4357/aa7261)
- 972 Araya, M. 2018a, *MNRAS*, 474, 102,
973 doi: [10.1093/mnras/stx2779](https://doi.org/10.1093/mnras/stx2779)
- 974 —. 2018b, *ApJ*, 859, 69,
975 doi: [10.3847/1538-4357/aabd7e](https://doi.org/10.3847/1538-4357/aabd7e)
- 976 Arsioli, B., & Polenta, G. 2018, *Astron.*
977 *Astrophys.*, 616, A20,
978 doi: [10.1051/0004-6361/201832786](https://doi.org/10.1051/0004-6361/201832786)
- 979 Atwood, W., Albert, A., Baldini, L., et al. 2013,
980 ArXiv:1303.3514.
981 <https://arxiv.org/abs/1303.3514>
- 982 Atwood, W. B., Abdo, A. A., Ackermann, M.,
983 et al. 2009, *ApJ*, 697, 1071,
984 doi: [10.1088/0004-637X/697/2/1071](https://doi.org/10.1088/0004-637X/697/2/1071)
- 985 Ballet, J., et al. 2015, in *ICRC*, Vol. 34, ICRC
986 2015, ed. A. S. Borisov et al., 848
- 987 Bird, A. J., Bazzano, A., Malizia, A., et al. 2016,
988 *ApJS*, 223, 15,
989 doi: [10.3847/0067-0049/223/1/15](https://doi.org/10.3847/0067-0049/223/1/15)
- 990 Bregeon, J., Charles, E., & Wood, M. 2013,
991 ArXiv:1304.5456.
992 <https://arxiv.org/abs/1304.5456>
- 993 Bruel, P., Burnett, T. H., Digel, S. W., et al. 2018,
994 arXiv:1810.11394.
995 <https://arxiv.org/abs/1810.11394>
- 996 Buehler, R., Scargle, J. D., Blandford, R. D.,
997 et al. 2012, *ApJ*, 749, 26,
998 doi: [10.1088/0004-637X/749/1/26](https://doi.org/10.1088/0004-637X/749/1/26)
- 999 Capetti, A., Massaro, F., & Baldi, R. D. 2017a,
1000 *A&A*, 598, A49,
1001 doi: [10.1051/0004-6361/201629287](https://doi.org/10.1051/0004-6361/201629287)
- 1002 —. 2017b, *A&A*, 601, A81,
1003 doi: [10.1051/0004-6361/201630247](https://doi.org/10.1051/0004-6361/201630247)
- 1004 Caputo, R., Buckley, M. R., Martin, P., et al.
1005 2016, *PhRvD*, 93, 062004,
1006 doi: [10.1103/PhysRevD.93.062004](https://doi.org/10.1103/PhysRevD.93.062004)
- 1007 Casandjian, J.-M., & Grenier, I. A. 2008, *A&A*,
1008 489, 849, doi: [10.1051/0004-6361:200809685](https://doi.org/10.1051/0004-6361:200809685)
- 1009 Chang, Y.-L., Arsioli, B., Giommi, P., &
1010 Padovani, P. 2017, *A&A*, 598, A17,
1011 doi: [10.1051/0004-6361/201629487](https://doi.org/10.1051/0004-6361/201629487)
- 1012 Chaty, S., Fortin, F., & Garcia, F. 2018, in
1013 preparation
- 1014 Condon, J. J., Cotton, W. D., Greisen, E. W.,
1015 et al. 1998, *AJ*, 115, 1693, doi: [10.1086/300337](https://doi.org/10.1086/300337)

- 1016 Coronado, J., Domínguez, A., & Sánchez-Conde,
1017 M. A. 2019
1018 D'Abrusco, R., Massaro, F., Paggi, A., et al. 2014,
1019 ApJS, 215, 14,
1020 doi: [10.1088/0067-0049/215/1/14](https://doi.org/10.1088/0067-0049/215/1/14)
1021 de Ruiter, H. R., Willis, A. G., & Arp, H. C. 1977,
1022 A&AS, 28, 211
1023 Devin, J., Acero, F., Ballet, J., & Schmid, J. 2018,
1024 A&A, 617, A5,
1025 doi: [10.1051/0004-6361/201833008](https://doi.org/10.1051/0004-6361/201833008)
1026 Ferrand, G., & Safi-Harb, S. 2012, *Advances in*
1027 *Space Research*, 49, 1313,
1028 doi: [10.1016/j.asr.2012.02.004](https://doi.org/10.1016/j.asr.2012.02.004)
1029 Górski, K. M., Hivon, E., Banday, A. J., et al.
1030 2005, ApJ, 622, 759, doi: [10.1086/427976](https://doi.org/10.1086/427976)
1031 Green, D. A. 2014, *Bulletin of the Astronomical*
1032 *Society of India*, 42, 47.
1033 <https://arxiv.org/abs/1409.0637>
1034 Griffin, R. D., Dai, X., & Thompson, T. A. 2016,
1035 ApJL, 823, L17,
1036 doi: [10.3847/2041-8205/823/1/L17](https://doi.org/10.3847/2041-8205/823/1/L17)
1037 Grondin, M.-H., Funk, S., Lemoine-Goumard, M.,
1038 et al. 2011, ApJ, 738, 42,
1039 doi: [10.1088/0004-637X/738/1/42](https://doi.org/10.1088/0004-637X/738/1/42)
1040 H. E. S. S. Collaboration, Abdalla, H.,
1041 Abramowski, A., et al. 2018, A&A, 612, A6,
1042 doi: [10.1051/0004-6361/201629790](https://doi.org/10.1051/0004-6361/201629790)
1043 Hanabata, Y., Katagiri, H., Hewitt, J. W., et al.
1044 2014, ApJ, 786, 145,
1045 doi: [10.1088/0004-637X/786/2/145](https://doi.org/10.1088/0004-637X/786/2/145)
1046 Harris, W. E. 1996, AJ, 112, 1487,
1047 doi: [10.1086/118116](https://doi.org/10.1086/118116)
1048 Hartman, R. C., Bertsch, D. L., Bloom, S. D.,
1049 et al. 1999, ApJS, 123, 79, doi: [10.1086/313231](https://doi.org/10.1086/313231)
1050 Hayashida, M., Stawarz, Ł., Cheung, C. C., et al.
1051 2013, ApJ, 779, 131,
1052 doi: [10.1088/0004-637X/779/2/131](https://doi.org/10.1088/0004-637X/779/2/131)
1053 Healey, S. E., Romani, R. W., Cotter, G., et al.
1054 2008, ApJS, 175, 97, doi: [10.1086/523302](https://doi.org/10.1086/523302)
1055 Healey, S. E., Romani, R. W., Taylor, G. B., et al.
1056 2007, ApJS, 171, 61, doi: [10.1086/513742](https://doi.org/10.1086/513742)
1057 HI4PI Collaboration, Ben Bekhti, N., Flöer, L.,
1058 et al. 2016, A&A, 594, A116,
1059 doi: [10.1051/0004-6361/201629178](https://doi.org/10.1051/0004-6361/201629178)
1060 Hu, F., & Zidek, J. V. 2002, *Canad. J. Statist.*,
1061 30, 347
1062 Johannesson, G., Orlando, E., & the Fermi-LAT
1063 collaboration. 2013, ArXiv:1307.0197.
1064 <https://arxiv.org/abs/1307.0197>
1065 Katagiri, H., Tibaldo, L., Ballet, J., et al. 2011,
1066 ApJ, 741, 44, doi: [10.1088/0004-637X/741/1/44](https://doi.org/10.1088/0004-637X/741/1/44)
1067 Katagiri, H., Yoshida, K., Ballet, J., et al. 2016a,
1068 ApJ, 818, 114,
1069 doi: [10.3847/0004-637X/818/2/114](https://doi.org/10.3847/0004-637X/818/2/114)
1070 Katagiri, H., Sugiyama, S., Ackermann, M., et al.
1071 2016b, ApJ, 831, 106,
1072 doi: [10.3847/0004-637X/831/1/106](https://doi.org/10.3847/0004-637X/831/1/106)
1073 Katsuta, J., Uchiyama, Y., Tanaka, T., et al.
1074 2012, ApJ, 752, 135,
1075 doi: [10.1088/0004-637X/752/2/135](https://doi.org/10.1088/0004-637X/752/2/135)
1076 Kerr, M. 2010, PhD thesis, University of
1077 Washington, ArXiv:1101:6072.
1078 <https://arxiv.org/abs/1101:6072>
1079 Kuźmicz, A., Jamroz, M., Bronarska, K.,
1080 Janda-Boczar, K., & Saikia, D. J. 2018, ApJS,
1081 238, 9, doi: [10.3847/1538-4365/aad9ff](https://doi.org/10.3847/1538-4365/aad9ff)
1082 Lande, J., Ackermann, M., Allafort, A., et al.
1083 2012, ApJ, 756, 5,
1084 doi: [10.1088/0004-637X/756/1/5](https://doi.org/10.1088/0004-637X/756/1/5)
1085 Li, J., Rea, N., Torres, D. F., & de Oña-Wilhelmi,
1086 E. 2017a, ApJ, 835, 30,
1087 doi: [10.3847/1538-4357/835/1/30](https://doi.org/10.3847/1538-4357/835/1/30)
1088 Li, J., Torres, D. F., Cheng, K. S., et al. 2017b,
1089 ApJ, 846, 169, doi: [10.3847/1538-4357/aa7fff](https://doi.org/10.3847/1538-4357/aa7fff)
1090 Liu, Q. Z., van Paradijs, J., & van den Heuvel,
1091 E. P. J. 2007, *VizieR Online Data Catalog*, 346,
1092 90807
1093 Manchester, R. N., Hobbs, G. B., Teoh, A., &
1094 Hobbs, M. 2005, AJ, 129, 1993,
1095 doi: [10.1086/428488](https://doi.org/10.1086/428488)
1096 Massaro, E., Giommi, P., Leto, C., et al. 2009,
1097 A&A, 495, 691,
1098 doi: [10.1051/0004-6361:200810161](https://doi.org/10.1051/0004-6361:200810161)
1099 Mattox, J. R., Bertsch, D. L., Chiang, J., et al.
1100 1996, ApJ, 461, 396, doi: [10.1086/177068](https://doi.org/10.1086/177068)
1101 Mattox, J. R., Wagner, S. J., Malkan, M., et al.
1102 1997, ApJ, 476, 692, doi: [10.1086/303639](https://doi.org/10.1086/303639)
1103 Mauch, T., Murphy, T., Buttery, H. J., et al.
1104 2003, MNRAS, 342, 1117,
1105 doi: [10.1046/j.1365-8711.2003.06605.x](https://doi.org/10.1046/j.1365-8711.2003.06605.x)
1106 McConnachie, A. W. 2012, AJ, 144, 4,
1107 doi: [10.1088/0004-6256/144/1/4](https://doi.org/10.1088/0004-6256/144/1/4)
1108 Mereghetti, S., Palombara, N. L., Tiengo, A.,
1109 et al. 2011, ApJ, 737, 51,
1110 doi: [10.1088/0004-637x/737/2/51](https://doi.org/10.1088/0004-637x/737/2/51)
1111 Murphy, T., Sadler, E. M., Ekers, R. D., et al.
1112 2010, MNRAS, 402, 2403,
1113 doi: [10.1111/j.1365-2966.2009.15961.x](https://doi.org/10.1111/j.1365-2966.2009.15961.x)

- 1114 Napier, P. J., Bagri, D. S., Clark, B. G., et al.
 1115 1994, IEEE Proceedings, 82, 658
- 1116 Nolan, P. L., Abdo, A. A., Ackermann, M., et al.
 1117 2012, ApJS, 199, 31,
 1118 doi: [10.1088/0067-0049/199/2/31](https://doi.org/10.1088/0067-0049/199/2/31)
- 1119 Oh, K., Koss, M., Markwardt, C. B., et al. 2018,
 1120 The Astrophysical Journal Supplement Series,
 1121 235, 4, doi: [10.3847/1538-4365/aaa7fd](https://doi.org/10.3847/1538-4365/aaa7fd)
- 1122 Peng, F.-K., Wang, X.-Y., Liu, R.-Y., Tang,
 1123 Q.-W., & Wang, J.-F. 2016, ApJL, 821, L20,
 1124 doi: [10.3847/2041-8205/821/2/L20](https://doi.org/10.3847/2041-8205/821/2/L20)
- 1125 Petrov, L., Mahony, E. K., Edwards, P. G., et al.
 1126 2013, MNRAS, 432, 1294,
 1127 doi: [10.1093/mnras/stt550](https://doi.org/10.1093/mnras/stt550)
- 1128 Pittori, C., Verrecchia, F., Chen, A. W., et al.
 1129 2009, A&A, 506, 1563,
 1130 doi: [10.1051/0004-6361/200911783](https://doi.org/10.1051/0004-6361/200911783)
- 1131 Pivato, G., Hewitt, J. W., Tibaldo, L., et al. 2013,
 1132 ApJ, 779, 179,
 1133 doi: [10.1088/0004-637X/779/2/179](https://doi.org/10.1088/0004-637X/779/2/179)
- 1134 Planck Collaboration, Aghanim, N., Ashdown, M.,
 1135 Aumont, J., et al. 2016, A&A, 596, A109,
 1136 doi: [10.1051/0004-6361/201629022](https://doi.org/10.1051/0004-6361/201629022)
- 1137 Popov, S. B., Mereghetti, S., Blinnikov, S. I.,
 1138 Kuranov, A. G., & Yungelson, L. R. 2018,
 1139 MNRAS, 474, 2750, doi: [10.1093/mnras/stx2910](https://doi.org/10.1093/mnras/stx2910)
- 1140 Porter, T. A., Jóhannesson, G., & Moskalenko,
 1141 I. V. 2017, ApJ, 846, 67,
 1142 doi: [10.3847/1538-4357/aa844d](https://doi.org/10.3847/1538-4357/aa844d)
- 1143 Rakshit, S., Stalin, C. S., Chand, H., & Zhang,
 1144 X.-G. 2017, ApJS, 229, 39,
 1145 doi: [10.3847/1538-4365/aa6971](https://doi.org/10.3847/1538-4365/aa6971)
- 1146 Sanders, D. B., Mazzarella, J. M., Kim, D.-C.,
 1147 Surace, J. A., & Soifer, B. T. 2003, AJ, 126,
 1148 1607, doi: [10.1086/376841](https://doi.org/10.1086/376841)
- 1149 Schinzel, F. K., Petrov, L., Taylor, G. B., &
 1150 Edwards, P. G. 2017, ApJ, 838, 139,
 1151 doi: [10.3847/1538-4357/aa6439](https://doi.org/10.3847/1538-4357/aa6439)
- 1152 Schinzel, F. K., Petrov, L., Taylor, G. B., et al.
 1153 2015, ApJS, 217, 4,
 1154 doi: [10.1088/0067-0049/217/1/4](https://doi.org/10.1088/0067-0049/217/1/4)
- 1155 Schmidt, K., Priebe, A., & Boller, T. 1993,
 1156 Astronomische Nachrichten, 314, 371
- 1157 Shahbaz, T., & Watson, C. A. 2007, A&A, 474,
 1158 969, doi: [10.1051/0004-6361:20078251](https://doi.org/10.1051/0004-6361:20078251)
- 1159 Smith, D. A., Bruel, P., Cognard, I., et al. 2019,
 1160 ApJ, 871, 78, doi: [10.3847/1538-4357/aaf57d](https://doi.org/10.3847/1538-4357/aaf57d)
- 1161 Stappers, B. W., Archibald, A. M., Hessels,
 1162 J. W. T., et al. 2014, ApJ, 790, 39,
 1163 doi: [10.1088/0004-637X/790/1/39](https://doi.org/10.1088/0004-637X/790/1/39)
- 1164 Tang, Q.-W., Wang, X.-Y., & Tam, P.-H. T. 2014,
 1165 ApJ, 794, 26, doi: [10.1088/0004-637X/794/1/26](https://doi.org/10.1088/0004-637X/794/1/26)
- 1166 Véron-Cetty, M.-P., & Véron, P. 2010, A&A, 518,
 1167 A10, doi: [10.1051/0004-6361/201014188](https://doi.org/10.1051/0004-6361/201014188)
- 1168 Voges, W., Aschenbach, B., Boller, T., et al. 1999,
 1169 A&A, 349, 389
- 1170 —. 2000, VizieR Online Data Catalog, 9029
- 1171 Yeung, P. K. H., Kong, A. K. H., Tam, P. H. T.,
 1172 et al. 2017, ApJ, 837, 69,
 1173 doi: [10.3847/1538-4357/aa5df1](https://doi.org/10.3847/1538-4357/aa5df1)
- 1174 —. 2016, ApJ, 827, 41,
 1175 doi: [10.3847/0004-637X/827/1/41](https://doi.org/10.3847/0004-637X/827/1/41)
- 1176 Yoast-Hull, T. M., Gallagher, John S., I., Aalto,
 1177 S., & Varenius, E. 2017, MNRAS, 469, L89,
 1178 doi: [10.1093/mnrasl/slx054](https://doi.org/10.1093/mnrasl/slx054)
- 1179 Zanin, R., Fernández-Barral, A., de Oña
 1180 Wilhelmi, E., et al. 2016, A&A, 596, A55,
 1181 doi: [10.1051/0004-6361/201628917](https://doi.org/10.1051/0004-6361/201628917)
- 1182 Zdziarski, A. A., Malyshev, D., Chernyakova, M.,
 1183 & Pooley, G. G. 2017, MNRAS, 471, 3657,
 1184 doi: [10.1093/mnras/stx1846](https://doi.org/10.1093/mnras/stx1846)
- 1185 Zhang, P. F., Xin, Y. L., Fu, L., et al. 2016,
 1186 MNRAS, 459, 99, doi: [10.1093/mnras/stw567](https://doi.org/10.1093/mnras/stw567)

APPENDIX

A. WEIGHTED LOG-LIKELIHOOD

1187

1188

1189 In 3FGL we introduced a first attempt at accounting for systematic errors in the maximum
 1190 likelihood process itself, at the source detection level. It was not used in the source characterization,
 1191 however, for lack of a suitable framework. The standard way to account for systematic errors (for
 1192 example in *XSPEC*²²) is to define them as a fraction ϵ of the signal and add them to the statistical
 1193 errors in quadrature, in a χ^2 formalism. This can be adapted to the maximum likelihood framework
 1194 by introducing weights $w_i < 1$ (Hu & Zidek 2002) as

$$\log \mathcal{L} = \sum_i w_i (n_i \log M_i - M_i) \tag{A1}$$

1195 where M_i and n_i are the model and observed counts in each bin, and the sum runs over all bins
 1196 in space and energy. The source significance can then be quantified in the same way, via the Test
 1197 Statistic $TS = 2 \log(\mathcal{L}/\mathcal{L}_0)$ in which \mathcal{L} and \mathcal{L}_0 are the (weighted) likelihood with and without the
 1198 source of interest, respectively.

1199 Since the statistical variance in Poisson statistics is the signal itself, a first guess for the weights
 1200 could be

$$w_i = \frac{M_i}{M_i + (\epsilon M_i)^2} = \frac{1}{1 + \epsilon^2 M_i} \tag{A2}$$

1201 However, that formulation has a serious flaw, which is that it is not stable to rebinning. If one splits
 1202 the bins in half, then M_i is split in half while ϵ stays the same (it is defined externally). In the limit
 1203 of very small bins, obviously the weights will all tend to 1 and the $\log \mathcal{L}$ formula will tend to the
 1204 unweighted one, even though nothing has changed in the underlying data or the model.

1205 The solution we propose, originally presented in Ballet et al. (2015), is to define a suitable integral
 1206 over energy (E) and space (\mathbf{r}) $N(\mathbf{r}, E)$ which does not depend on binning. M_i in the weight formula
 1207 is then replaced by $N(\mathbf{r}_i, E_i)$ taken at the event's coordinates. For the integral over space, since the
 1208 catalog mostly deals with point sources, the logical solution is to integrate the background under the
 1209 PSF, i.e., convolve the model with the PSF $P(\mathbf{r}, E)$, normalized to 1 at the peak (this is equivalent,
 1210 for a flat diffuse emission, to multiplying by the PSF solid angle). Note that the model already
 1211 contains the PSF, so this amounts to applying a double convolution to the sky model.

1212 For the energy integral the choice is less obvious. The source spectrum is not a narrow line, so
 1213 convolving with the energy dispersion (similar to what is done for space) is not justified. An integral
 1214 over the full energy range would give the same weight to all energies, which is clearly not what we
 1215 want (there is no reason to downplay the few high-energy events). The option we adopt here is to
 1216 start the integration at the current energy.

$$w_i = \frac{1}{1 + \epsilon^2 N(\mathbf{r}_i, E_i)} \tag{A3}$$

$$N(\mathbf{r}_i, E_i) = \int_{E_i}^{E_{\max}} S(\mathbf{r}_i, E) dE \tag{A4}$$

$$S(\mathbf{r}, E) = \frac{dM}{dE}(\mathbf{r}, E) * P(\mathbf{r}, E) \tag{A5}$$

²² <https://heasarc.gsfc.nasa.gov/xanadu/xspec/>

1217 where dM/dE is the differential model. As energy increases, the spectra (in counts) decrease and
 1218 the LAT PSF gets narrower so the convolution makes S even steeper than dM/dE . As a result, the
 1219 integral giving N is nearly always dominated by the lowest energies, so the exact upper bound E_{\max}
 1220 is not critical. The only spectral region where it is important is the very lowest energies (< 100 MeV)
 1221 where the effective area rises steeply. In order not to penalize the lowest energies too much, we set
 1222 $E_{\max} = 2E_i$ in Eq A4.

1223 There are two possibilities to define dM/dE . Since the main origin of the systematic error is the
 1224 diffuse emission, we can restrict dM/dE to the diffuse emission model only (we call the result model-
 1225 based weights). On the other hand there are also systematic uncertainties on sources due to PSF
 1226 calibration and our imperfect spectral representation, so another option is to enter the full model (or
 1227 the data themselves) into dM/dE (we call the result data-based weights). That second choice limits
 1228 spurious sources next to bright sources. There is of course no reason why the level of systematics ϵ
 1229 should be the same for the diffuse emission model and the sources, but in practice it is a reasonable
 1230 approximation.

1231 Another important point, for the procedure to be stable, is that the weights should not change
 1232 with the model parameters. So dM/dE must be defined beforehand (for example from a previous
 1233 fit). In this work we use data-based weights computed from the data themselves, with a common ϵ .
 1234 The data are not as smooth as the model, but this is not a problem in the regime of large counts
 1235 where weights play a role.

1236 We assume here that ϵ is a true constant (it depends neither on space nor on energy). For a given
 1237 ϵ the weights are close to 1 at high energy and decrease toward low energy. At a given energy the
 1238 weights are smallest where the model is largest (in the Galactic ridge). Considering all event types
 1239 (not what we do in 4FGL), for 8 years and $\epsilon = 3\%$, at 100 MeV the weights are everywhere less than
 1240 12%. They reach 50% at high latitude at 250 MeV, and 90% at 500 MeV. In the Galactic ridge, the
 1241 weights are 0.5% at 100 MeV, 1.5% at 250 MeV, 5% at 500 MeV, 20% at 1 GeV, 60% at 2 GeV and
 1242 reach 90% at 4.5 GeV.

1243 There remains a specific difficulty, due to the fact that at a given energy we split the data into
 1244 several components, each corresponding to a particular event type (with a different PSF). Since the
 1245 systematics play in the same way on all components, the weights must be computed globally (i.e.,
 1246 weights must be lower when using PSF2 and PSF3 events than when using PSF3 alone). On the
 1247 other hand, the resulting uncertainties with two components should be smaller than those with a
 1248 single component (adding a second one adds information). In this work, we started by computing
 1249 weights w_k individually for each component k (the dependence on E and \mathbf{r} is left implicit). Then we
 1250 assumed that the final weights are simply proportional to the original ones, with a factor $\alpha < 1$ (α
 1251 depends on E and \mathbf{r} as well). A reasonable solution is then

$$N_{\min} = \min_k N_k \quad (\text{A6})$$

$$K_{\text{tot}} = \sum_k \left(\frac{N_{\min}}{N_k} \right)^2 \quad (\text{A7})$$

$$\alpha = \frac{1 + \epsilon^2 N_{\min}}{1 + \epsilon^2 N_{\min} K_{\text{tot}}} \quad (\text{A8})$$

$$w_k = \frac{\alpha}{1 + \epsilon^2 N_k} \quad (\text{A9})$$

¹²⁵² K_{tot} and α are 1 if one component dominates over the others, and K_{tot} is the number of components
¹²⁵³ if they are all similar.

¹²⁵⁴ B. DESCRIPTION OF THE FITS VERSION OF THE 4FGL CATALOG

Table 9. LAT 4FGL FITS Format: LAT_Point_Source_Catalog Extension

Column	Format	Unit	Description
Source_Name	18A	...	Source name 4FGL JHHMM.m+DDMMa ^a
RAJ2000	E	deg	Right Ascension
DEJ2000	E	deg	Declination
GLON	E	deg	Galactic Longitude
GLAT	E	deg	Galactic Latitude
Conf_95_SemiMajor	E	deg	Long radius of error ellipse at 95% confidence
Conf_95_SemiMinor	E	deg	Short radius of error ellipse at 95% confidence
Conf_95_PosAng	E	deg	Position angle (eastward) of the long axis from celestial North
ROI_num	I	...	RoI number (cross-reference to ROIs extension)
Extended_Source_Name	18A	...	Cross-reference to the ExtendedSources extension
Signif_Avg	E	...	Source significance in σ units over the 100 MeV to 1 TeV band
Pivot_Energy	E	MeV	Energy at which error on differential flux is minimal
Flux1000	E	$\text{cm}^{-2} \text{s}^{-1}$	Integral photon flux from 1 to 100 GeV
Unc_Flux1000	E	$\text{cm}^{-2} \text{s}^{-1}$	1σ error on integral photon flux from 1 to 100 GeV
Energy_Flux100	E	$\text{erg cm}^{-2} \text{s}^{-1}$	Energy flux from 100 MeV to 100 GeV obtained by spectral fitting
Unc_Energy_Flux100	E	$\text{erg cm}^{-2} \text{s}^{-1}$	1σ error on energy flux from 100 MeV to 100 GeV
SpectrumType	18A	...	Spectral type in the global model (PowerLaw, LogParabola, PLSuperExpCutoff)
PL_Flux_Density	E	$\text{cm}^{-2} \text{MeV}^{-1} \text{s}^{-1}$	Differential flux at Pivot_Energy in PowerLaw fit
Unc_PL_Flux_Density	E	$\text{cm}^{-2} \text{MeV}^{-1} \text{s}^{-1}$	1σ error on PL_Flux_Density
PL_Index	E	...	Photon index when fitting with PowerLaw
Unc_PL_Index	E	...	1σ error on PL_Index
LP_Flux_Density	E	$\text{cm}^{-2} \text{MeV}^{-1} \text{s}^{-1}$	Differential flux at Pivot_Energy in LogParabola fit
Unc_LP_Flux_Density	E	$\text{cm}^{-2} \text{MeV}^{-1} \text{s}^{-1}$	1σ error on LP_Flux_Density
LP_Index	E	...	Photon index at Pivot_Energy (α of Eq. 2) when fitting with LogParabola
Unc_LP_Index	E	...	1σ error on LP_Index
LP_beta	E	...	Curvature parameter (β of Eq. 2) when fitting with LogParabola
Unc_LP_beta	E	...	1σ error on LP_beta
LP_SigCurv	E	...	Significance (in σ units) of the fit improvement between PowerLaw and LogParabola. A value greater than 4 indicates significant curvature
PLEC_Flux_Density	E	$\text{cm}^{-2} \text{MeV}^{-1} \text{s}^{-1}$	Differential flux at Pivot_Energy in PLSuperExpCutoff fit
Unc_PLEC_Flux_Density	E	$\text{cm}^{-2} \text{MeV}^{-1} \text{s}^{-1}$	1σ error on PLEC_Flux_Density
PLEC_Index	E	...	Low-energy photon index (Γ of Eq. 3) when fitting with PLSuperExpCutoff
Unc_PLEC_Index	E	...	1σ error on PLEC_Index
PLEC_Expfactor	E	...	Exponential factor (a of Eq. 3) when fitting with PLSuperExpCutoff
Unc_PLEC_Expfactor	E	...	1σ error on PLEC_Expfactor
PLEC_Exp_Index	E	...	Exponential index (b of Eq. 3) when fitting with PLSuperExpCutoff
Unc_PLEC_Exp_Index	E	...	1σ error on PLEC_Exp_Index
PLEC_SigCurv	E	...	Same as LP_SigCurv for PLSuperExpCutoff model
Npred	E	...	Predicted number of events in the model
ASSOC_GAM	18A	...	Correspondence to previous γ -ray source catalog ^b
TEVCAT_FLAG	A	...	P if positional association with non-extended source in TeVCat

Table 9 continued on next page

Table 9 (*continued*)

Column	Format	Unit	Description
			E if associated with an extended source in TeVCat, N if no TeV association
ASSOC_TEV	24A	...	Name of likely corresponding TeV source from TeVCat, if any
CLASS	5A	...	Class designation for associated source; see Table 7
ASSOC1	28A	...	Name of identified or likely associated source
ASSOC2	26A	...	Alternate name or indicates whether the source is inside an extended source
ASSOC_PROB_BAY	E	...	Probability of association according to the Bayesian method ^c
ASSOC_PROB_LR	E	...	Probability of association according to the Likelihood Ratio method ^c
RA_Counterpart	D	deg	Right Ascension of the counterpart ASSOC1
DEC_Counterpart	D	deg	Declination of the counterpart ASSOC1
Unc_Counterpart	E	deg	95% precision of the counterpart localization ^d
Flags	I	...	Source flags (binary coding as in Table 5) ^e

^aThe letter at the end can be **e** (extended source), **i** (for Crab nebula inverse Compton) or **s** (for Crab nebula synchrotron).

^bin the order 3FHL > 3FGL > 2FHL > 1FHL > 2FGL > 1FGL > 0FGL.

^cProbabilities < 0.8 are formally set to 0.

^dFor extended counterparts, this reports their extension radius.

^eEach condition is indicated by one bit among the 16 bits forming **Flags**. The bit is raised (set to 1) in the dubious case, so that sources without any warning sign have **Flags** = 0.

1255 The FITS format version of the early release of the 4FGL catalog has five binary table extensions.
 1256 The extension **LAT_Point_Source_Catalog_Extension** has all of the information about the sources.
 1257 Its format is described in Table 9.

1258 The extension **GTI** is a standard Good-Time Interval listing the precise time intervals (start and
 1259 stop in Mission Elapsed Time) included in the data analysis. The number of intervals is fairly large
 1260 because on most orbits (~95 min) *Fermi* passes through the South Atlantic Anomaly (SAA), and
 1261 science data taking is stopped during these times. In addition, data taking is briefly interrupted
 1262 on each non-SAA-crossing orbit, as *Fermi* crosses the ascending node. Filtering of time intervals
 1263 with large rocking angles, gamma-ray bursts, solar flares, data gaps, or operation in non-standard
 1264 configurations introduces some more entries. The GTI is provided for reference and would be useful,
 1265 e.g., for reconstructing the precise data set that was used for the analysis.

1266 The extension **ExtendedSources** (format unchanged since 2FGL) contains information about the
 1267 75 spatially extended sources that are modeled in the 4FGL source list (§ 3.4), including locations
 1268 and shapes. The extended sources are indicated by an **e** appended to their names in the main table.
 1269 The extension **ROIs** contains information about the 1748 RoIs over which the analysis ran. In
 1270 particular it reports the best-fit diffuse parameters. Its format is very close to that in 3FGL, with
 1271 one exception. The **RADIUS** column is replaced by **CoreRadius** which reports the radius of the RoI
 1272 core (in which the sources which belong to the RoI are located). The RoI radius (half-width in binned
 1273 mode) depends on the component, and is given by the core radius plus **RingWidth**, where the latter
 1274 is given in the **Components** extension.

1275 The extension **Components** is new to 4FGL. It reports the settings of each individual component
 1276 (15 in all) whose sum forms the entire data set for the SummedLikelihood approach, as described in
 1277 Table 2. Its format is given by Table 10.

Table 10. LAT 4FGL FITS Format: Components Extension

Column	Format	Unit	Description
Emin	E	MeV	Lower bound of component's energy interval
Emax	E	MeV	Upper bound of component's energy interval
ENumBins	I	...	Number of bins inside energy interval
EvType	I	...	Event type selection for this component
ZenithCut	E	deg	Maximum zenith angle for this component
RingWidth	E	deg	Difference between RoI radius and core radius
PixelSize	E	deg	Pixel size for this component (of exposure map in unbinned mode)
BinnedMode	I	...	0=Unbinned, 1=Binned
Weighted	I	...	1 if weights were applied to this component